Available online at www.sciencedirect.com
SCIENCE DIRECT®
Comput. Methods Appl. Mech. Engrg. 195 (2006) 4732–4752
Computer methods in applied mechanics and engineering
www.elsevier.com/locate/cma

A comparative study on finite elements for capturing strong discontinuities: E-FEM vs X-FEM

J. Oliver [a,*], A.E. Huespe [a], P.J. Sánchez [b]

[a] E.T.S. d'Enginyers de Camins, Canals i Ports, Technical University of Catalonia (UPC), Campus Nord UPC, Mòdul C-1, c/Jordi Girona 1-3, 08034 Barcelona, Spain
[b] CIMEC, CONICET, Güemes 3450, 3000 Santa Fe, Argentina

Received 8 March 2005; received in revised form 20 September 2005; accepted 20 September 2005

Abstract

A comparative study on finite elements for capturing strong discontinuities by means of elemental (E-FEM) or nodal enrichments (X-FEM) is presented. Based on the same constitutive model (continuum damage) and linear elements (triangles and tetrahedra) optimized implementations of both types of enrichments in the same non-linear code are tested for a representative set of 2D and 3D crack propagation examples. It is shown that both methods provide the same qualitative and quantitative results for enough refined meshes. For the performed tests, E-FEM exhibited, in general, a higher accuracy, mostly for coarse meshes, whereas, convergence rate with mesh refinement, which is super-linear, showed slightly higher for X-FEM. As for the computational costs for single crack modelling X-FEM showed, depending on the case, from 1.1 to about 2.5 times more expensive than E-FEM. For multiple cracks, the computational cost of E-FEM keeps constant, whereas the cost associated to X-FEM increases linearly with the number of modelled cracks.

Keywords: Finite elements with embedded discontinuities; E-FEM; X-FEM; Computational material failure; Strong discontinuities

1. Motivation

In recent years finite elements with discontinuities have gained increasing interest in modelling material failure, due to their specific ability to provide, unlike standard finite elements, specific kinematics to capture strong discontinuities. They essentially consist of enriching the (continuous) displacement modes of the standard finite elements, with additional (discontinuous) displacements, devised for capturing the physical discontinuity i.e.: fractures, cracks, slip lines, etc. The discontinuity path is placed inside the elements irrespective of the size and specific orientation of them. Then, typical drawbacks of standard finite elements in modelling displacement discontinuities, like spurious mesh size and mesh bias dependences, can be effectively removed. In addition, unlike with standard elements, mesh refinement is not strictly necessary to capture those discontinuities, and the simulation can be done with relatively coarse meshes. By using that technology, in conjunction with some additional refinements, realistic simulations of multiple strong discontinuities propagating in three-dimensional bodies can be achieved, with small computers, in reasonable computational times.

As for the enriching technique, two broad families can be distinguished in terms of the support of the enriching discontinuous displacement modes:

* Corresponding author. Fax: +34 93 401 1048.
E-mail address: xavier.oliver@upc.es (J. Oliver).

0045-7825/$ - see front matter © 2005 Elsevier B.V. All rights reserved.
doi:10.1016/j.cma.2005.09.020

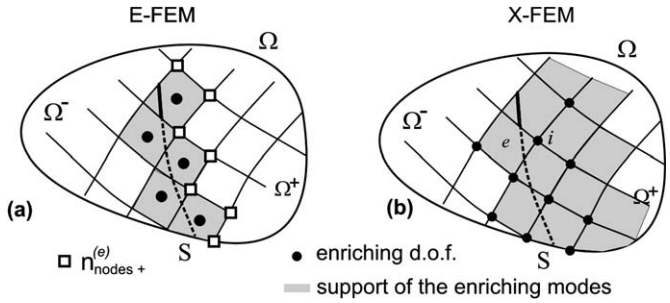

Fig. 1. Nodal and elemental enrichments.

- *Elemental enrichment* [1,2,7,8,10,18–20,22,29,34]: the support for each mode is a given element, see Fig. 1a. For the purposes of identification of this kind of enrichment, in the remaining of this work it will be termed as E-FEM enrichment.
- *Nodal enrichment* [4,5,16,17,33,35]: the support of each mode is the one of a given nodal shape function i.e.: those elements surrounding a specific node, see Fig. 1b. Most of the formulations of this family, available in the literature, have been developed in the context of the partition of unity methods, of a broader scope, under the name of X-FEM method [5]. Therefore, this name will be assigned, in this work, to this kind of enrichment.

To the best of the authors' knowledge, a rigorous comparative study on both families of elements and their relative performance is still lacking. At the most, some speculative statements about the behaviour of each method have been made from every author's experience and feeling, but quantitative aspects about relative errors, rates of convergence with mesh refinement, and computational cost are not yet available. This is the purpose of this work: to assess the relative performance of both types of enrichments in terms of those aspects that can be quantitatively measured through numerical tests and simulations; covering a wide range of cases: two-dimensional and three-dimensional simulations and single and multiple fracturing. In order to make the comparison as fair as possible, the best (intending to be the most effective) numerical implementation for every case has been implemented in the same numerical simulation code [15]. In this sense, the implicit–explicit procedure, presented elsewhere [24–26], has been used to integrate the constitutive model. This procedure renders positive definite and constant, in every time step, the algorithmic stiffness matrix of the linearized problem, even in presence of strain softening; convergence of the non-linear problem is always achieved in just one iteration per time step and, therefore, the time advancing procedure is completely robust and the same number of iterations in every implementation is guaranteed as the number of time steps is imposed.

Then, for a selected set of numerical tests, results have been obtained using the same basic element (linear triangles or tetrahedra) elementary or nodal enriched by discontinuous displacement modes and using exactly the same data: finite element mesh, material properties, time advancing algorithm, number of time steps, linearization procedure etc. Finally, representative action–response curves, measures of the accuracy, and records of the computational cost have been obtained for each case and used for comparison purposes.

The remainder of this work has been structured as follows: in Section 2 the fundamentals of E-FEM and X-FEM enrichments are presented; in Section 3 details of the comparison setting, in terms of the constitutive model and numerical implementation aspects, are given. Then, in Section 4, results obtained with both formulations, for a number of representative examples, are systematically compared in terms of accuracy, convergence and computational cost. Finally, in Section 5, conclusions about this comparative study are obtained.

2. Problem formulation

Let us consider the typical material failure problem in solid mechanics, exhibiting cracks or slip lines modes in the spatial domain Ω (see Fig. 2), which are characterized by the following discontinuous displacement field:

$$\mathbf{u}(\mathbf{x}) = \bar{\mathbf{u}}(\mathbf{x}) + \mathscr{H}_S(\mathbf{x})\boldsymbol{\beta}(\mathbf{x}); \quad \mathscr{H}_S(\mathbf{x}) = \begin{cases} 1 & \forall \mathbf{x} \in \Omega^+, \\ 0 & \forall \mathbf{x} \in \Omega^-, \end{cases} \tag{1}$$

where $\mathbf{u}$ stands for the displacement field, $\bar{\mathbf{u}}$ and $\boldsymbol{\beta}$ are, respectively, the regular displacement field and the displacement jump and $\mathscr{H}_S(\mathbf{x})$ stands for the Heaviside (step) function shifted to the discontinuity interface S. For the infinitesimal strain case and introducing generalized functions, the strain field compatible with Eq. (1) results:

$$\boldsymbol{\varepsilon}(\mathbf{x}) = \nabla^{\text{sym}}\mathbf{u} = \nabla^{\text{sym}}\bar{\mathbf{u}}(\mathbf{x}) + \mathscr{H}_S\nabla^{\text{sym}}\boldsymbol{\beta}(\mathbf{x}) + \delta_S[\mathbf{n}(\mathbf{x}) \otimes \boldsymbol{\beta}(\mathbf{x})]^{\text{sym}}, \tag{2}$$

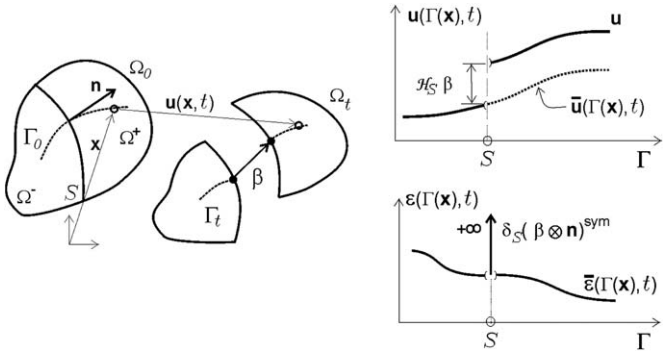

Fig. 2. Strong discontinuity kinematics.

where $\mathbf{n}$ is normal to S and δ_S stands for the Dirac's delta-function shifted to S. For the spatially discretized body, Ω^h, the variational governing equation, in the standard form and in absence of body forces, reads:

$$\int_{\Omega^h} \nabla^{\mathrm{sym}}\delta\mathbf{u}^h\cdot\boldsymbol{\sigma}\,\mathrm{d}\Omega = \int_{\Gamma_\sigma^h}\delta\mathbf{u}^h\cdot\bar{\mathbf{t}}\,\mathrm{d}\Gamma_\sigma \quad \forall\delta\mathbf{u}^h\in\mathscr{V}_0^h, \tag{3}$$

where $\Gamma_\sigma^h\subset\partial\Omega^h$ is the boundary with prescribed tractions, $\bar{\mathbf{t}}$, and $\mathscr{V}_0^h$ is the space of admissible displacements, which should be appropriately defined. Both the displacement field (1) and the space $\mathscr{V}_0^h$ are represented in different ways by the elemental and nodal embedded strong discontinuity enrichments.

2.1. X-FEM enrichment

The space of interpolation functions is defined by

$$\mathscr{V}^h_{\text{X-FEM}} = \left\{\mathbf{u}^h(\mathbf{x})\,|\,\mathbf{u}^h(\mathbf{x}) = \sum_{i=1}^{n_{\text{node}}}(N_i(\mathbf{x})\mathbf{d}_i + \mathscr{H}_S N_i(\mathbf{x})\boldsymbol{\beta}_i)\right\}, \tag{4}$$

N_i standing for the standard interpolation finite element shape functions, $\mathbf{d}_i$ are the nodal regular displacement vector, $\boldsymbol{\beta}_i$ is the nodal displacement jump vector and n_{node} is the number of nodes of the finite element mesh. The corresponding (infinitesimal) strain field results:

$$\boldsymbol{\varepsilon}^h(\mathbf{x}) = \nabla^{\mathrm{sym}}\mathbf{u}^h = \sum_{i=1}^{n_{\text{node}}}[(\nabla N_i\otimes\mathbf{d}_i)^{\mathrm{sym}} + \mathscr{H}_S(\nabla N_i\otimes\boldsymbol{\beta}_i)^{\mathrm{sym}} + \delta_S(\mathbf{n}\otimes N_i\boldsymbol{\beta}_i)^{\mathrm{sym}}]. \tag{5}$$

Then the variations, with respect to parameters $(\mathbf{d}_i,\boldsymbol{\beta}_i)$ in Eq. (4) lead to the discrete equilibrium equations:

$$\begin{aligned}
&\delta\mathbf{d}_i\cdot\left(\int_{\Omega^h}\nabla N_i\cdot\boldsymbol{\sigma}\,\mathrm{d}\Omega - \int_{\Gamma_\sigma^h}N_i\cdot\bar{\mathbf{t}}\,\mathrm{d}\Gamma\right) = 0 \quad \forall\delta\mathbf{d}_i;\ \ i=1,n_{\text{node}},\\
&\delta\boldsymbol{\beta}_i\cdot\left(\int_{\Omega^h}\mathscr{H}_S\nabla N_i\cdot\boldsymbol{\sigma}\,\mathrm{d}\Omega + \int_S N_i\cdot(\boldsymbol{\sigma}_S\cdot\mathbf{n})\mathrm{d}S\right) = 0 \quad \forall\delta\boldsymbol{\beta}_i;\ \ i=1,n_{\text{node}}.
\end{aligned} \tag{6}$$

The term $\boldsymbol{\sigma}_S\cdot\mathbf{n}=\mathbf{t}_S$, in Eq. (6b), can be interpreted as an interface cohesive traction.

2.2. E-FEM enrichment

In this approach, the discontinuous displacement is interpolated by using the following functional space:

$$\begin{aligned}
&\mathscr{V}^h_{\text{E-FEM}} = \left\{\mathbf{u}^h(\mathbf{x})\,|\,\mathbf{u}^h(\mathbf{x}) = \sum_{i=1}^{n_{\text{node}}}(N_i(\mathbf{x})\mathbf{d}_i) + \sum_{e=1}^{n_{\text{elem}}}\mathscr{M}_S^{(e)}\boldsymbol{\beta}_e\right\},\\
&\mathscr{M}_S^{(e)} = \mathscr{H}_S - \varphi^{(e)};\quad \varphi^{(e)} = \sum_{i=1}^{n^{(e)}_{\text{node}+}}N_i^{(e)},
\end{aligned} \tag{7}$$

where, n_{elem} is the number of elements and $n^{(e)}_{\text{node}+}$ refers to those nodes of element e placed in Ω^+ (see Fig. 1). In Eq. (7) $\boldsymbol{\beta}_e$ are degrees of freedom describing the elemental displacement jumps and $\mathscr{M}^{(e)}_S$ is the so-called elemental unit jump function whose support is the elemental domain $\Omega^{(e)}$ [28]. The corresponding strain field reads:

$$\boldsymbol{\varepsilon}^h(\mathbf{x}) = \nabla^{\text{sym}}\mathbf{u}^h = \sum_{i=1}^{n_{\text{node}}}(\nabla N_i \otimes \mathbf{d}_i)^{\text{sym}} - \sum_{e=1}^{n_{\text{elem}}}([(\nabla\varphi^{(e)} \otimes \boldsymbol{\beta}_e)^{\text{sym}} - \delta_S(\mathbf{n}\otimes\boldsymbol{\beta}_e)^{\text{sym}}]), \tag{8}$$

and variations, in Eq. (8), with respect to parameters $(\mathbf{d}_i, \boldsymbol{\beta}_e)$ lead to the discrete variational equations defining a *kinematically consistent* E-FEM implementation [10,13]:

$$\begin{aligned}
&\delta\mathbf{d}_i \cdot \left(\int_{\Omega^h} \nabla N_i \cdot \boldsymbol{\sigma}\,\mathrm{d}\Omega - \int_{\Gamma^h_\sigma} N_i \cdot \bar{\mathbf{t}}\,\mathrm{d}\Gamma\right) = 0 \quad \forall\delta\mathbf{d}_i;\ \ i = 1, n_{\text{node}},\\
&\delta\boldsymbol{\beta}_e \cdot \left(\int_{\Omega^{(e)}} \nabla\varphi^{(e)} \cdot \boldsymbol{\sigma}\,\mathrm{d}\Omega + \int_{S^{(e)}} (\boldsymbol{\sigma}_S \cdot \mathbf{n})\,\mathrm{d}S\right) = 0 \quad \forall\delta\boldsymbol{\beta}_e;\ \ e = 1, n_{\text{elem}}.
\end{aligned} \tag{9}$$

3. Comparison setting

In order to make a rigorous comparison, a common comparison setting for both methods has to be defined in terms of the constitutive model, the numerical algorithms and the finite element implementation. This is described in next sections.

3.1. Constitutive model: degenerated traction-separation law

For the sake of simplicity, an isotropic continuum damage model, equipped with strain softening, has been chosen to model the mechanical behaviour of the material. The essentials of the model are the following:

$$\begin{aligned}
&\varphi(\boldsymbol{\varepsilon}, r) = \frac{1}{2}\frac{q(r)}{r}(\boldsymbol{\varepsilon} : \mathbf{C} : \boldsymbol{\varepsilon}) = \frac{1}{2}\frac{q(r)}{r}(\bar{\lambda}\,\mathrm{tr}^2(\boldsymbol{\varepsilon}) + 2\mu\boldsymbol{\varepsilon} : \boldsymbol{\varepsilon}),\\
&\boldsymbol{\sigma} = \frac{\partial\varphi(\boldsymbol{\varepsilon}, r)}{\partial\boldsymbol{\varepsilon}} = \underbrace{\frac{q}{r}}_{1-d}\ \mathbf{C} : \boldsymbol{\varepsilon} = (1-d)\ \underbrace{\mathbf{C} : \boldsymbol{\varepsilon}}_{\bar{\boldsymbol{\sigma}}(\boldsymbol{\varepsilon})\ \text{(effective stress)}} = (1-d)\bar{\boldsymbol{\sigma}}\\
&\dot{r} = \gamma; \quad r(t)|_{t=t_0} \equiv r_0 = \frac{\sigma_u}{\sqrt{E}},\\
&\dot{q} = H(q)\dot{r}; \quad q(t)|_{t=t_0} \equiv q_0 = r_0,\\
&\gamma \geqslant 0; \quad \mathsf{F}_\sigma(\boldsymbol{\sigma}, q) \leqslant 0; \quad \gamma\mathsf{F}_\sigma = 0,\\
&\mathsf{F}_\sigma(\boldsymbol{\sigma}, q) = \tau_\sigma - q; \quad \tau_\sigma = \underbrace{\sqrt{\boldsymbol{\sigma}^+ : \mathbf{C}^{-1} : \boldsymbol{\sigma}}}_{\text{equivalent stress}} = \frac{q}{r}\underbrace{\sqrt{\bar{\boldsymbol{\sigma}}^+(\boldsymbol{\varepsilon}) : \mathbf{C}^{-1} : \bar{\boldsymbol{\sigma}}(\boldsymbol{\varepsilon})}}_{\text{equivalent strain } \tau_\varepsilon},
\end{aligned} \tag{10}$$

where $\varphi(\boldsymbol{\varepsilon}, r)$ is the free energy, depending on the strain tensor $\boldsymbol{\varepsilon}$, and the internal variable r, $\mathbf{C} = \bar{\lambda}(\mathbf{1}\otimes\mathbf{1}) + 2\mu\mathbf{I}$ is the elastic constitutive tensor, where $\bar{\lambda}$ and μ are the Lame's parameters and $\mathbf{1}$ and $\mathbf{I}$ are the identity tensors of second and fourth order, respectively. In Eq. (10) $d = 1 - q(r)/r$ is the continuum damage variable, $\boldsymbol{\sigma}$ stands for the stress tensor and $\bar{\boldsymbol{\sigma}} = \mathbf{C} : \boldsymbol{\varepsilon}$ is the effective stress tensor. Its positive counterpart is then defined as

$$\bar{\boldsymbol{\sigma}}^+ = \sum_{i=1}^{i=3}\langle\bar{\sigma}_i\rangle\mathbf{p}_i \otimes \mathbf{p}_i, \tag{11}$$

where $\langle\bar{\sigma}_i\rangle$ stands for the positive part (Mac Auley bracket) of the ith principal effective stress $\bar{\sigma}_i$ ($\langle\bar{\sigma}_i\rangle = \bar{\sigma}_i$ for $\bar{\sigma}_i > 0$ and $\langle\bar{\sigma}_i\rangle = 0$ for $\bar{\sigma}_i < 0$) and $\mathbf{p}_i$ stands for the ith stress eigenvector. The initial elastic domain in the damage model is defined as $E^0_{\boldsymbol{\sigma}} := \{\boldsymbol{\sigma}; \sqrt{\boldsymbol{\sigma}^+ \cdot \mathbf{C}^{e^{-1}} \cdot \boldsymbol{\sigma}} < r_0\}$ and, therefore, it is unbounded for compressive stress states ($\boldsymbol{\sigma}^+ = \mathbf{0}$) so that damage becomes only associated to tensile stress states as it is usual for modelling tensile failure in quasi-brittle materials. Material softening is defined by the evolution of the internal variable $q(r)$ in terms of the continuum softening modulus $H(q) \leqslant 0$. Finally, σ_u and E are, respectively, the tensile strength and the Young's modulus. One of the advantages of the previous model, infrequent in non-linear constitutive models, is that the internal variable r can be integrated in closed form as

$$r(t) = \max_{s\in[0,t]} \tau_\varepsilon(\boldsymbol{\varepsilon}(s), r_0) \tag{12}$$

and, from this, the complete constitutive model can be analytically integrated from Eq. (10).

In the context of the continuum strong discontinuity approach (CSDA) the preceding constitutive model should be adapted to return bounded stresses when the singular (unbounded) strain field (2) is introduced into the standard continuum context. This regularization is achieved by substituting the Dirac's delta function δ_S by a regularized sequence, $\delta_S \equiv \mu_S/k$ $(k \to 0)$, where $\mu_S(\mathbf{x})$ is a collocation function on the discontinuity interface $S(\mu_S(\mathbf{x}) = 1\ \forall \mathbf{x} \in S$ and $\mu_S(\mathbf{x}) = 0$ otherwise). In addition, the continuum softening modulus, H, in Eq. (10), is reinterpreted, in the distributional sense [32] and, then, regularized as

$$H(q) = k\overline{H}(q) \tag{13}$$

in terms of a discrete softening modulus $\overline{H}$, considered a material property available from the mechanical and fracturing properties of the material (peak stress σ_u, Young modulus E, and fracture energy G_f; see [21,27] for additional details).

In this context it can be shown [21] that the following traction separation law, relating the traction, $\mathbf{t}_S = \boldsymbol{\sigma}_S \cdot \mathbf{n}$, and the displacement jump, $\boldsymbol{\beta}$, is automatically fulfilled at the discontinuity interface S after activation of the strong discontinuity kinematics (2):

$$\begin{aligned}
&\varphi_S(\boldsymbol{\beta},\alpha) = \frac{1}{2}\frac{q(\alpha)}{\alpha}[\boldsymbol{\beta} : \mathbf{Q}^e : \boldsymbol{\beta}] = \frac{1}{2}\frac{q(\alpha)}{\alpha}[(\bar{\lambda}+\mu)(\boldsymbol{\beta}\cdot\mathbf{n})^2 + \mu\boldsymbol{\beta}\cdot\boldsymbol{\beta}],\\
&\mathbf{Q}^e = \mathbf{n}\cdot\mathbf{C}\cdot\mathbf{n} = (\bar{\lambda}+\mu)\mathbf{n}\otimes\mathbf{n} + \mu\mathbf{1},\\
&\mathbf{t}_S = \frac{\partial\varphi_S(\boldsymbol{\beta},\alpha)}{\partial\boldsymbol{\beta}} = \underbrace{\frac{q}{\alpha}}_{1-\omega}\mathbf{Q}^e\cdot\boldsymbol{\beta} = (1-\omega)\mathbf{Q}^e\cdot\boldsymbol{\beta},\\
&\dot{\alpha} = \dot{\gamma}; \quad \alpha(t)|_{t=t_{\mathrm{loc}}} = 0,\\
&\dot{q} = \overline{H}(q)\alpha; \quad q(t)|_{t=t_{\mathrm{loc}}} \equiv q_{\mathrm{loc}},\\
&\dot{\gamma} \geqslant 0; \quad \mathsf{F}_t(\mathbf{t},q) \leqslant 0; \quad \dot{\gamma}\mathsf{F}_t = 0,\\
&\mathsf{F}_t(\mathbf{t},q) = \tau_t - q; \quad \tau_t = \underbrace{\sqrt{\mathbf{t}_S\cdot(\mathbf{Q}^e)^{-1}\cdot\mathbf{t}_S}}_{\text{equivalent traction}},\\
&(\mathbf{t}_S = \boldsymbol{\sigma}_S\cdot\mathbf{n}; \mathbf{t}_S^+ = \boldsymbol{\sigma}_S^+\cdot\mathbf{n}),
\end{aligned} \tag{14}$$

where $\varphi_S = \lim_{k\to 0}(k\varphi(\boldsymbol{\varepsilon}_S, r_S))$ is the free energy density per unit of area at the discontinuity interface, q and $\alpha = \lim_{k\to 0} r$ are the internal variables, and t_{loc} stands for the localization time or the time of activation of the traction separation law (see Section 3.3). The (discrete) model in Eq. (14) is said to be a projection (degeneration) of the continuum model in Eq. (10) onto the discontinuity interface S. There are, in fact, two options to do so:

- A *continuum implementation* of the model (10), $\boldsymbol{\sigma}(\boldsymbol{\varepsilon}(\bar{\boldsymbol{\varepsilon}},\boldsymbol{\beta}))$, into the variational equations (6) and (9). This is the procedure followed in the continuum strong discontinuity approach (CSDA) [27].
- A *discrete implementation*, based on the substitution of the traction separation law (14), $\mathbf{t}_S(\boldsymbol{\beta})$, in the term $\boldsymbol{\sigma}_S\cdot\mathbf{n}$ in the variational equations (6) and (9). This is the procedure followed in the discrete strong discontinuity approach (DSDA), see for instance [2].

Due to the equivalence of both models, the results obtained with the first option will only differ from the ones obtained with the second one in accounting for those volume dissipation mechanisms taking place before the localization time, t_{loc}. In this comparison study, the first option (continuum implementation) has been chosen, for both E-FEM and X-FEM enrichments, and considered representative of both implementation procedures.

3.2. Finite element implementation

Linear elements (triangles in 2D and tetrahedra in 3D) are selected as the basic elements to be enriched. Since one of the most relevant issues to be compared is the computational cost, a fairly optimized numerical implementation and coding of the mathematical models has been intended for both enrichments. In this sense, the E-FEM enriching degrees of freedom are condensed out at elemental level. As for X-FEM, those nodal degrees of freedom associated to the enriching modes, and the memory allocated to the corresponding dimensions of the elemental matrices, are exclusively activated for those nodes belonging to elements of the mesh that are intersected by the discontinuity path, and only after the time that failure in those elements is detected. Moreover, the additional nodal degrees of freedom are numbered as to minimize their impact on the banded structure of the resulting stiffness matrix. The remaining elements are computed following the classical implementation without enrichment.

As for the specific integration rules, they are sketched in Fig. 3. For the linear triangle and E-FEM enrichment two integration points have been considered, one corresponding to the regular domain $\Omega^{(e)}/S^{(e)}$ and the other to the singular

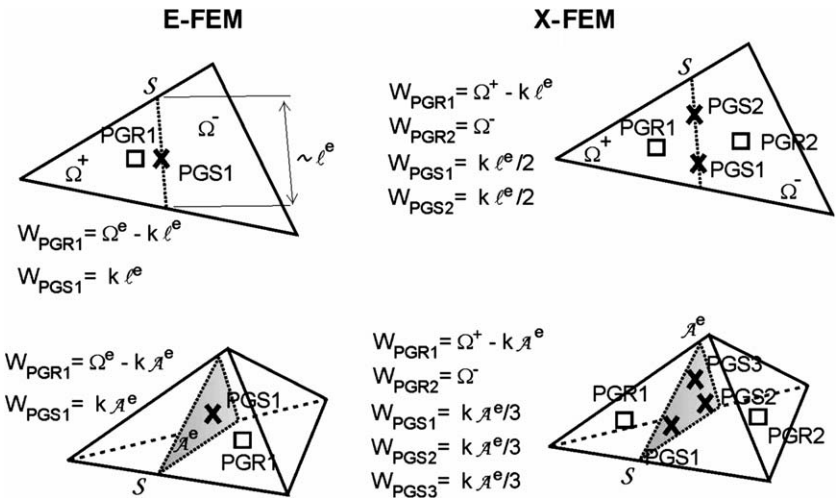

Fig. 3. Integration rules for E-FEM and X-FEM in 2D and 3D cases.

domain $S^{(e)}$. The X-FEM triangular element requires four Gauss-points (two regular and two singular) whose weights, w_{PG}, are shown in the same figure.

For 3D tetrahedron two sampling points (one regular and one singular) in E-FEM, and five sampling points in X-FEM (two regular and three singular) have been adopted. The accuracy of the three-points integration rule at $S^{(e)}$, for X-FEM in tetrahedra, when the elemental singular domain is a quadrilateral instead of a triangle, has been assessed by comparison with the, theoretically exact, four points rule. No substantial difference was found and the three sampling points were adopted in all cases to reduce computational time and implementation costs. Moreover, in order to minimize the impact on the computation of the higher integration order in the X-FEM formulation, this specific integration rule is only activated at those elements crossed by the discontinuity path. The remaining elements are, in both formulations, integrated using a single sampling point.

The value k in Fig. 3, is that parameter in the CSDA used to regularize the Dirac's delta function, δ_S, in Eqs. (5) and (8) (a very small parameter to which the results are insensitive, see Ref. [23]). Values ℓ^e and $\mathcal{A}^e$ correspond to the length (for 2D) and the area (for 3D) of the discontinuity path inside the element.

According to these specifications both, the E-FEM and X-FEM, elements have been inserted *in the same finite element code* for non-linear solid mechanic analysis [15]. Therefore, those ingredients of the analysis that are not specific of each of the compared methods (like time advancing schemes, tracking algorithms, continuation methods, non-linear solvers etc.) are common for both E-FEM and X-FEM implementations and they will not affect the relative performance of each method.

3.3. Propagation issues: determination of the discontinuity path

An important issue in the numerical solution of cracking problems in the CSDA is the correct prediction of the discontinuity path and, therefore, determination of those elements that have to be enriched with discontinuous modes. For this purposes several strategies (tracking algorithms [5,6,19,22] are available in the literature). In this comparison study a global tracking algorithm has been used on the basis of the following ingredients [23]:

- The normal to the propagation direction, $\mathbf{n}(\mathbf{x})$, at every material point $\mathbf{x}$, is determined, by resorting to the so-called *discontinuous bifurcation analysis* [36] based on the spectral properties of the localization tensor $\mathbf{Q}^{\text{loc}}$ as

$$\begin{cases} \mathbf{Q}^{\text{loc}}(\mathbf{x},t,\widehat{H},\hat{\mathbf{n}}) = \hat{\mathbf{n}}\cdot\mathbf{C}^{\text{tan}}(\widehat{H},\boldsymbol{\sigma}(\mathbf{x},t))\cdot\hat{\mathbf{n}}; \quad \|\hat{\mathbf{n}}\| = 1, \\ H^{\text{crit}}(\mathbf{x},t) = \max[\widehat{H};\exists\hat{\mathbf{n}}(\mathbf{x},\widehat{H},t) \mid \det\mathbf{Q}^{\text{loc}}(\mathbf{x},t,\widehat{H},\hat{\mathbf{n}}) = 0], \\ \tilde{\mathbf{n}}(\mathbf{x},t) = \hat{\mathbf{n}}(\mathbf{x},H^{\text{crit}},t), \end{cases}$$
$$t_{\text{loc}}(\mathbf{x}) \overset{\text{def}}{\equiv} \{H(\mathbf{x},t_{\text{loc}}) = H^{\text{crit}}(\mathbf{x},t_{\text{loc}})\},$$
$$\begin{cases} \mathbf{n}(\mathbf{x},t) = \tilde{\mathbf{n}}(\mathbf{x},t) & \forall t \leqslant t_{\text{loc}}(\mathbf{x}), \\ \mathbf{n}(\mathbf{x},t) = \tilde{\mathbf{n}}(\mathbf{x},t_{\text{loc}}) & \forall t \geqslant t_{\text{loc}}(\mathbf{x}), \end{cases} \tag{15}$$

where $\mathbf{C}^{\text{tan}}$ stands for the tangent constitutive operator, defining the incremental constitutive equation of the selected model ($\dot{\boldsymbol{\sigma}} = \mathbf{C}^{\text{tan}} : \dot{\boldsymbol{\varepsilon}}$), $H(\mathbf{x},t)$ is the softening modulus defined in Eq. (12), and $t_{\text{loc}}(\mathbf{x})$ is the localization time, i.e.: the time

as the chosen constitutive model becomes unstable allowing local bifurcation of the strain field and the formation of a weak discontinuity. It is characterized by the loss of positive definiteness of the localization tensor $\mathbf{Q}^{\text{loc}}$ in Eq. (15). Closed form formulas for determination of $\mathbf{n}$, for several families of constitutive models, can be found elsewhere [23,31,36]. The value of $\mathbf{n}(\mathbf{x}, t)$ is computed for every material point (the single elemental sampling point for numerical purposes) at every time step and it is frozen after the localization time, t_{loc}, of the element.

- Construction, at every time step, of the enveloping family (lines in 2D or surfaces in 3D) of the vector field orthogonal to $\mathbf{n}(\mathbf{x}, t)$ i.e.: the propagation vector field. This is done through a so-called *pseudo-thermal* algorithm (more details can be found in [22]). Then, those elements crossed by the same member (envelop) of that family and fulfilling the localization condition ($t(\mathbf{x}) \geqslant t_{\text{loc}}(\mathbf{x})$) are enriched with the discontinuous modes according to the respective E-FEM and X-FEM procedures.

3.4. Robustness issues. Implicit–explicit time integration scheme

It is a very well-known fact the lack of robustness typical of models involving strain softening in computational material failure. Even as the B.V.P. is mathematically well posed, the loss of the positive definite character of the tangent constitutive operator progressively deteriorates the algorithmic stiffness of the problem, as material failure propagates through the finite element mesh. As a consequence, the robustness of the convergence procedure for solving the non-linear problem is strongly affected and, in most cases, convergence can be achieved only by using very skilful procedures, which translate into large computational costs. In order to overcome this problem, an *implicit/explicit integration scheme*, presented elsewhere [24,25], for integration of the constitutive model has been adopted for both the E-FEM and X-FEM procedures. Two are the main advantages of that scheme:

- *The resulting algorithmic tangent operator is always positive definite*, which avoids the fundamental reasons for loss of robustness (at the cost of introducing an additional time-integration error in comparison with the standard implicit integration scheme). In consequence, a result is always obtained whatever is the length of the time step. The accuracy of the results can be then increased, and controlled, by shortening the length of the time step.
- *The resulting algorithmic tangent operator is constant* (for the adopted infinitesimal strain format) inside the time step. In consequence, convergence of the iteration procedure, to balance the internal and external forces, is achieved *in just one iteration per time step*.

The beneficial effects of that integration procedure in computations involving strain softening are dramatic, both in robustness and computational costs, as compared with the ones of the implicit scheme [24]. This is why, in the spirit, of using the best available algorithms for a fair comparison with the alternative, the explicit integration scheme has been adopted in this study for both the computations using E-FEM and X-FEM. In addition, and since robustness is almost complete, this guaranties the same number of time steps (and, therefore, of iterations) required to trace the response of a given problem with both methods, and makes the comparison completely objective in terms of accuracy and computational cost.

4. Numerical tests

In the computational setting defined in Section 3, the relative performances of the E-FEM vs. the X-FEM formulations are compared by solving a set of two- and three-dimensional material failure problems in concrete, for single or multiple crack cases. The following questions are aimed at being answered through this comparison:

- When applied to the same problem, do E-FEM and X-FEM provide the same (qualitative and quantitative) results?
- How do both formulations compare in terms of accuracy?
- What is their convergence rate with mesh refinement?
- What is their relative computational cost?

All the examples shown below have been run in a standard PC equipped with a single Pentium 4 – 3.0 GHz, 512 MB Ram – processor. As for comparison of the computational cost in the tables below, the following nomenclature has been adopted to identify some of the features and results for every problem:

- *Nstep*: number of time steps used for the complete analysis.
- Ne_{i}: number of initial equations (at the beginning of the analysis without any enriching degree of freedom).
- Ne_{f}: number of final equations (at the end of the analysis, including the additional enriching degrees of freedom).
- *RNe*: ratio of number of equations $Ne_{\text{f}}/Ne_{\text{i}}$.

- bw_i: initial average half bandwidth of the stiffness matrix.
- bw_f: final average half bandwidth of the stiffness matrix.
- Rbw: ratio of average bandwidths bw_f/bw_i.
- Ta: absolute CPU time for the problem (in seconds) for each formulation.
- RCC: relative computational cost (Ta with X-FEM/Ta with E-FEM).

4.1. Double-cantilever-beam (DCB) test with diagonal loads

The experimental test, reproduced in this section using two- and three-dimensional models, was reported in [11], and its numerical solution, in 2D, was also studied in [27,30].

Fig. 4 shows the geometric description, being the plate thickness 50.8 mm, and the spatial and temporal loading conditions. The diagonal compression forces, F_2, are initially introduced together with the wedge loads, F_1, increasing along the time, until reaching 3.78 kN. Then, the diagonal loads remain constant while the wedge loads increase. The material parameters are, Young's modulus: $E = 30{,}500$ MPa, Poisson's ratio: $\nu = 0.2$, fracture energy: $G_f = 100$ N/m, and ultimate tensile strength: $\sigma_u = 3$ MPa.

The choice of this test for comparison purposes lies on two reasons:

- The reported experimental crack path follows a flat surface (inclined 71° with the horizontal axis). Therefore, simulations can be made independent of the tracking procedure by imposing that specific crack path. This strategy has been followed in the 2D and 3D modelling, and, for the remaining examples of this work, the discontinuity path S has been determined by means of the global tracking procedure reported in Section 3.3.
- For 2D analyzes it is rather simple to construct structured meshes such that the discontinuity path intersects the elements in arbitrary directions. Those meshes will strongly challenge E-FEM formulations, which perform particularly well when the propagation direction is parallel to the element sides [10].

4.1.1. 2D modelling

A plane stress condition has been assumed. Convergence with mesh refinement has been analyzed by using a uniformly decreasing (in element size) sequence of meshes (S_1, S_2, S_3, S_4) in the fracture zone, with element sizes $h = 32$, 16, 8 and 4 mm, see Fig. 5.

Let $S^{efem} = \{S_1^{efem}, S_2^{efem}, S_3^{efem}, S_4^{efem}\}$ and $S^{xfem} = \{S_1^{xfem}, S_2^{xfem}, S_3^{xfem}, S_4^{xfem}\}$ be, respectively, the sequence of numerically obtained solutions using the E-FEM and the X-FEM. Load–displacement curves, for the E-FEM and X-FEM sequences, are plotted in Fig. 6a, for the E-FEM sequence, and in Fig. 6b, for the X-FEM. There, a clear qualitative convergence, with mesh refinement, in both cases is noticed.

Fig. 7 compares, for each couple of the two solution sequences, the results obtained by the E-FEM and X-FEM procedures. There it can be observed that the solutions provided by both methods converge to each other as the mesh is refined.

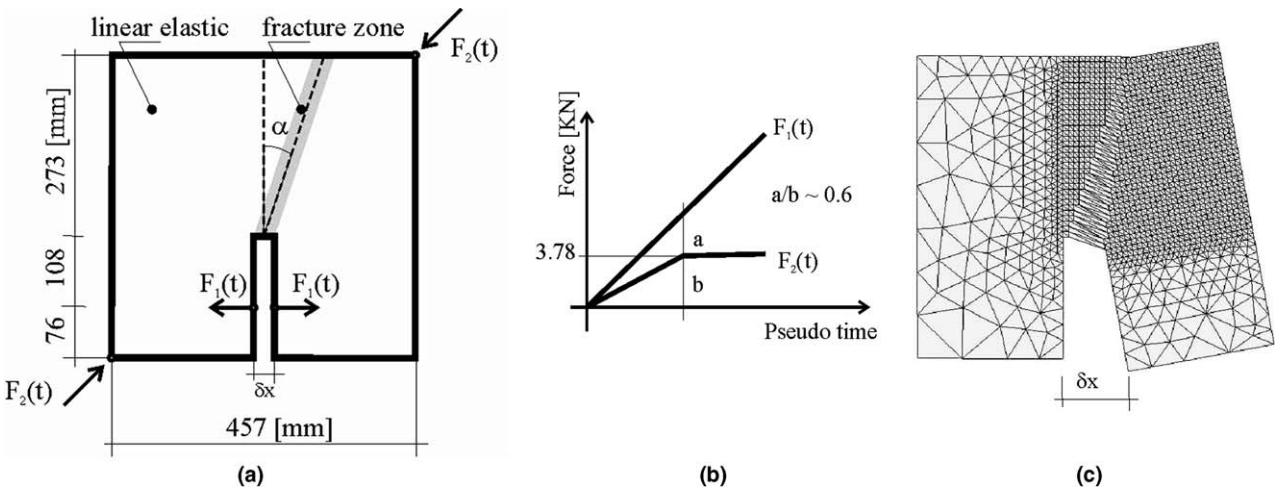

Fig. 4. Double-cantilever-beam (DCB) test with diagonal loads: (a) geometry and loading conditions, (b) loading history and (c) typical deformed mesh.

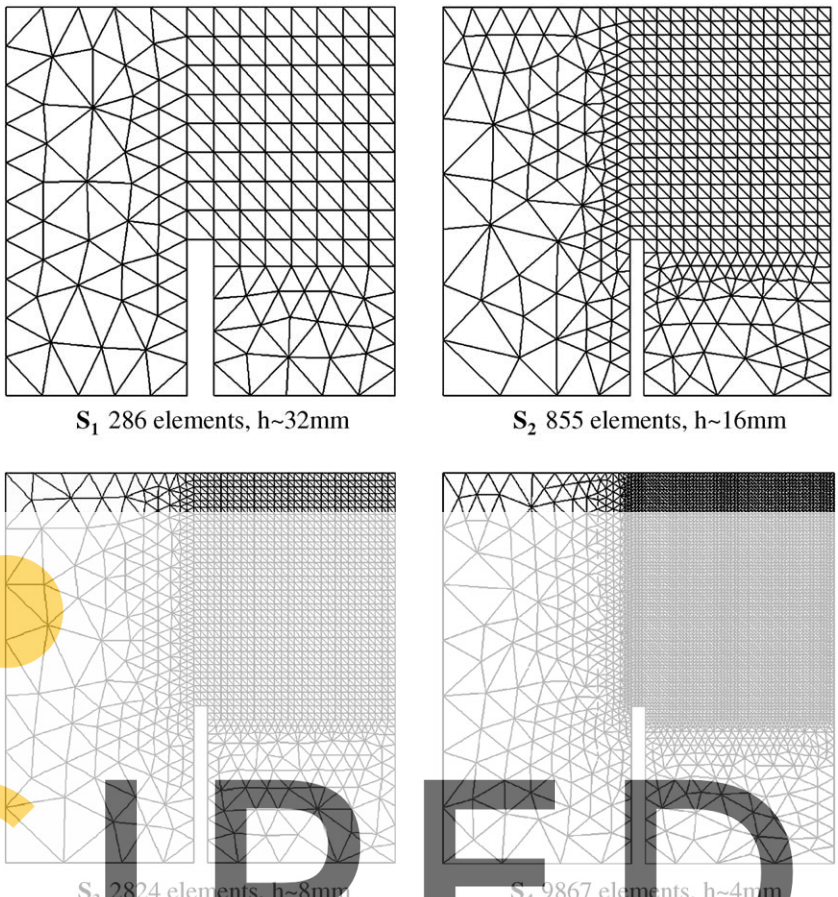

Fig. 5. 2D double-cantilever-beam (DCB) test with diagonal loads. Structured mesh sequence (S_1, S_2, S_3, S_4).

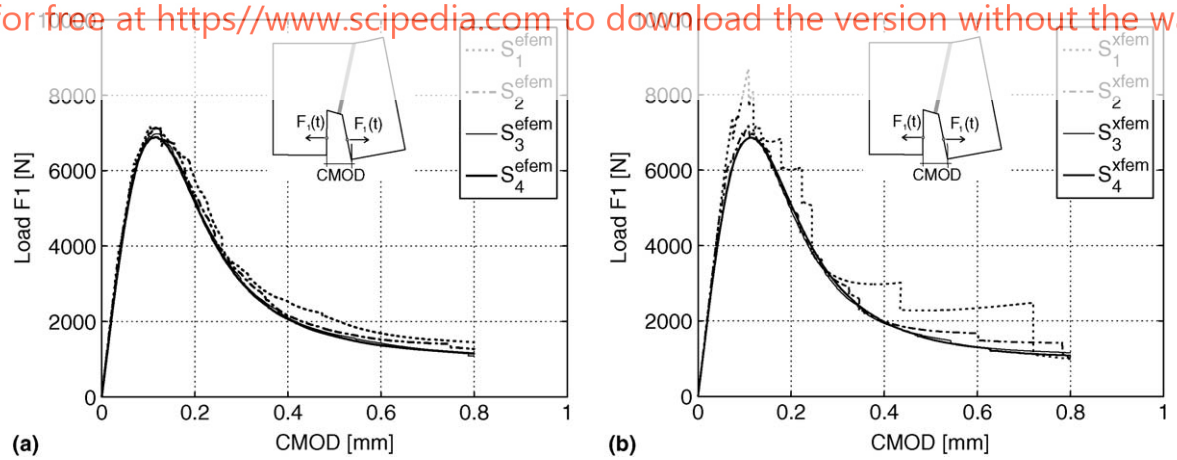

Fig. 6. 2D double-cantilever-beam (DCB) test with diagonal loads. Equilibrium curves (load F_1 vs. CMOD): (a) E-FEM and (b) X-FEM solutions.

However, in order to translate these qualitative observations into figures, L_2-*norms* of the differences are computed by means of the following formula:

$$\|e_{\mathrm{CMOD}_i}\|_{L_2} = \frac{\|S_i - S_{\mathrm{ref}}\|_{L_2}}{\|S_{\mathrm{ref}}\|_{L_2}} = \frac{\sqrt{\int_0^{\max(\mathrm{CMOD})} (S_i - S_{\mathrm{ref}})^2 \,\mathrm{d}x}}{\sqrt{\int_0^{\max(\mathrm{CMOD})} (S_{\mathrm{ref}})^2 \,\mathrm{d}x}}; \quad i = 1, 2, 3, \tag{16}$$

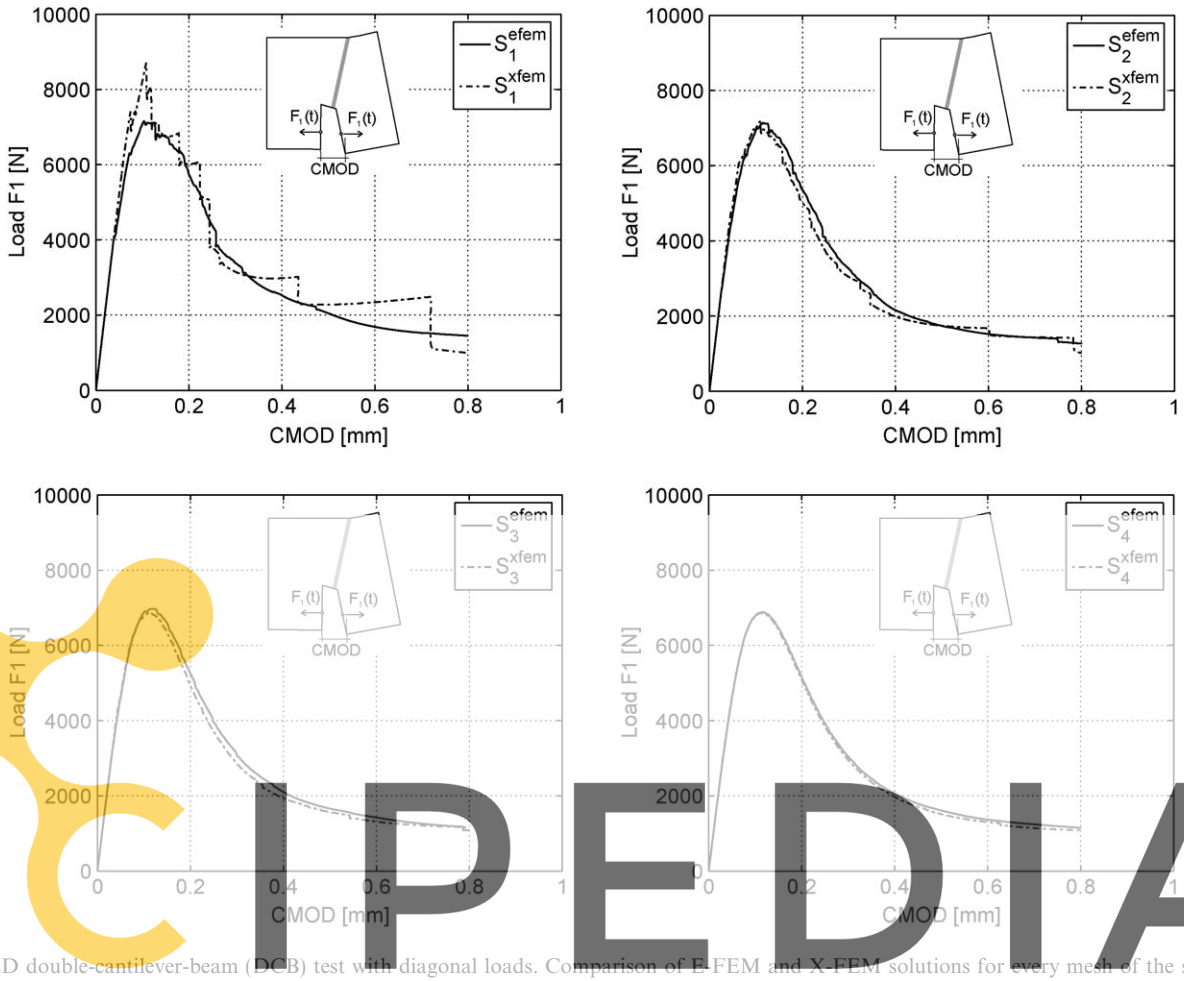

Fig. 7. 2D double-cantilever-beam (DCB) test with diagonal loads. Comparison of E-FEM and X-FEM solutions for every mesh of the sequence.

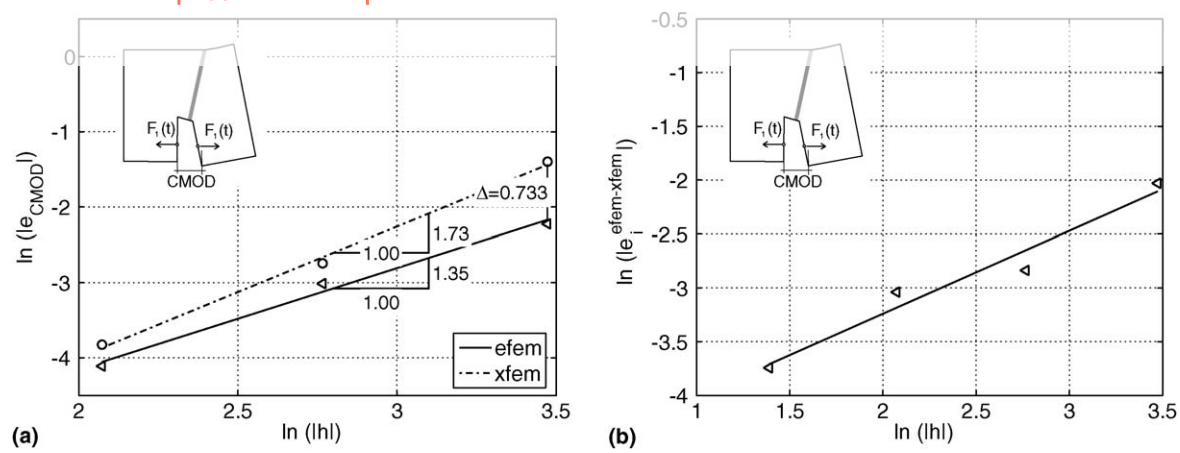

Fig. 8. 2D double-cantilever-beam (DCB) test with diagonal loads: (a) relative errors vs. element size and (b) E-FEM – X-FEM differences vs. element size h.

where $\|e_{\mathrm{CMOD}_i}\|_{L_2}$ stands for the relative error of solution S_i, in the L_2-*norms*, with respect to a reference (*exact*) solution S_{ref}. Since the exact solution is not available, the one obtained with the finer mesh is considered as the reference solution ($S_{\mathrm{ref}} \equiv S_4$). In Fig. 8a. the obtained relative errors with respect to the corresponding finite element size, h, for every discretization, are plotted in a log–log diagram (and fitted in a linear regression) for the E-FEM and X-FEM solutions. There, it can be clearly observed a *higher accuracy* for E-FEM, and that *both methods exhibit a super-linear convergence* (the slope of the regression curves is at the interior of the interval [1,2]).

The L_2-*norm* of the difference of solutions in the two sequences of solutions $S^{\text{efem}} = \{S_1^{\text{efem}}, S_2^{\text{efem}}, S_3^{\text{efem}}, S_4^{\text{efem}}\}$ and $S^{\text{xfem}} = \{S_1^{\text{xfem}}, S_2^{\text{xfem}}, S_3^{\text{xfem}}, S_4^{\text{xfem}}\}$ is obtained as

$$\|e_i^{\text{efem}-\text{xfem}}\|_{L_2} = \frac{\|S_i^{\text{efem}} - S_i^{\text{xfem}}\|_{L_2}}{\|S_i^{\text{xfem}}\|_{L_2}} = \frac{\sqrt{\int_0^{\max(\text{CMOD})} (S_i^{\text{efem}} - S_i^{\text{xfem}})^2 \, \mathrm{d}x}}{\sqrt{\int_0^{\max(\text{CMOD})} (S_i^{\text{xfem}})^2 \, \mathrm{d}x}}; \quad i = 1, \ldots, 4, \tag{17}$$

where now $\|e_i^{\text{efem}-\text{xfem}}\|_{L_2}$ is a measure of the difference of the solutions between the E-FEM and X-FEM procedures for the same mesh. In Fig. 8b the corresponding results are plotted in a log–log diagram and fitted with a linear regression. The clear reduction of the error with decreasing element size proves *the convergence of both formulations, with mesh refinement, to the same value* ($\lim_{h\to 0}(S_i^{\text{efem}} - S_i^{\text{xfem}}) = 0$).

Table 1 refers to the computational costs required for solving the problem, with both methods, for every mesh. Recalling that, in the last column, RCC refers to the relative computational cost, X-FEM/E-FEM, it can be clearly observed that *X-*

Table 1
2D double-cantilever-beam (DCB) test with diagonal loads

Finite element mesh (1)	*Nstep* (2)	Method (3)	Ne_{i} (4)	Ne_{f} (5)	*RNe* (6) = (5)/(4)	bw_{i} (7)	bw_{f} (8)	*Rbw* (9) = (8)/(7)	*Ta* [s] (10)	RCC (11)
Mesh 1 (286 elem.)	1415	E-FEM	343	343	1	22	22	1	26.2	1.24
		X-FEM	343	387	1.13	22	26	1.18	32.6	
Mesh 2 (855 elem.)	1610	E-FEM	935	935	1	42	42	1	93.1	1.21
		X-FEM	935	1027	1.10	42	47	1.12	113	
Mesh 3 (2824 elem.)	1610	E-FEM	2949	2949	1	59	59	1	344	1.15
		X-FEM	2949	3127	1.06	59	63	1.07	396	
Mesh 4 (9867 elem.)	1610	E-FEM	10,073	10,073	1	108	108	1	1675	1.12
		X-FEM	10,073	10,431	1.03	108	112	1.04	1882	

Computational data and relative computational cost X-EFEM/E-FEM (RCC).

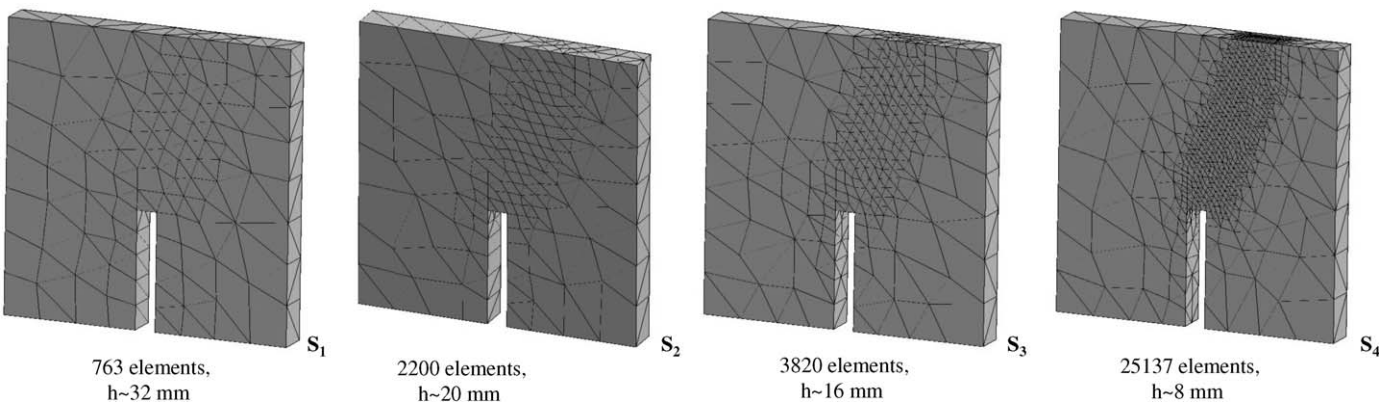

Fig. 9. 3D double-cantilever-beam (DCB) test with diagonal loads. Unstructured mesh sequence ($\mathbf{S}_1, \mathbf{S}_2, \mathbf{S}_3, \mathbf{S}_4$).

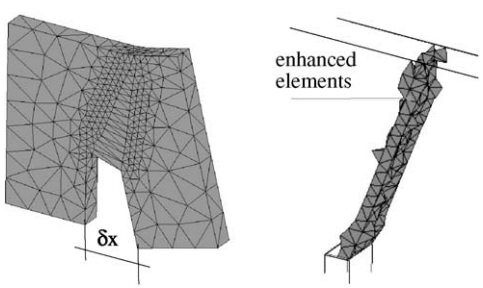

Fig. 10. 3D double-cantilever-beam (DCB) test with diagonal loads. Modelled crack path.

FEM is, *in all meshes*, *more expensive than E-FEM* though the relative extra cost tends to decrease as the mesh is refined. This is the general trend observed in all the analyzed examples in this work.

4.1.2. 3D modelling

The same test is now conducted in a 3D modelling. Four unstructured meshes, shown in Fig. 9, with average element sizes in the crack path zone $h = 32$, 20, 16 and 8 mm are used defining the mesh sequence $(\mathbf{S}_1, \mathbf{S}_2, \mathbf{S}_3, \mathbf{S}_4)$.

Fig. 10 shows the set of finite elements capturing the discontinuity in an advanced localization state corresponding to the maximum attained CMOD value.

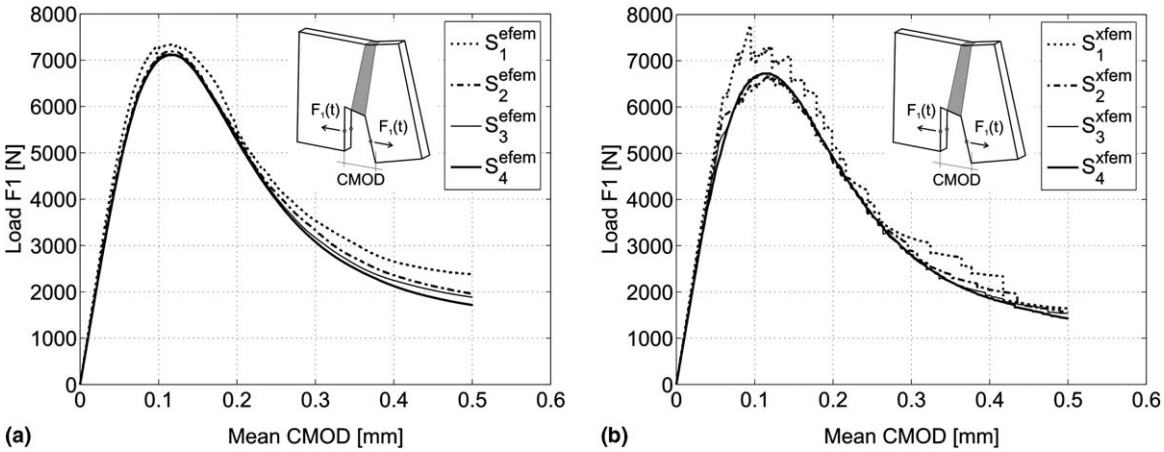

Fig. 11. 3D double-cantilever-beam (DCB) test with diagonal loads. Equilibrium curves (load F_1 vs. CMOD): (a) E-FEM and (b) X-FEM solutions.

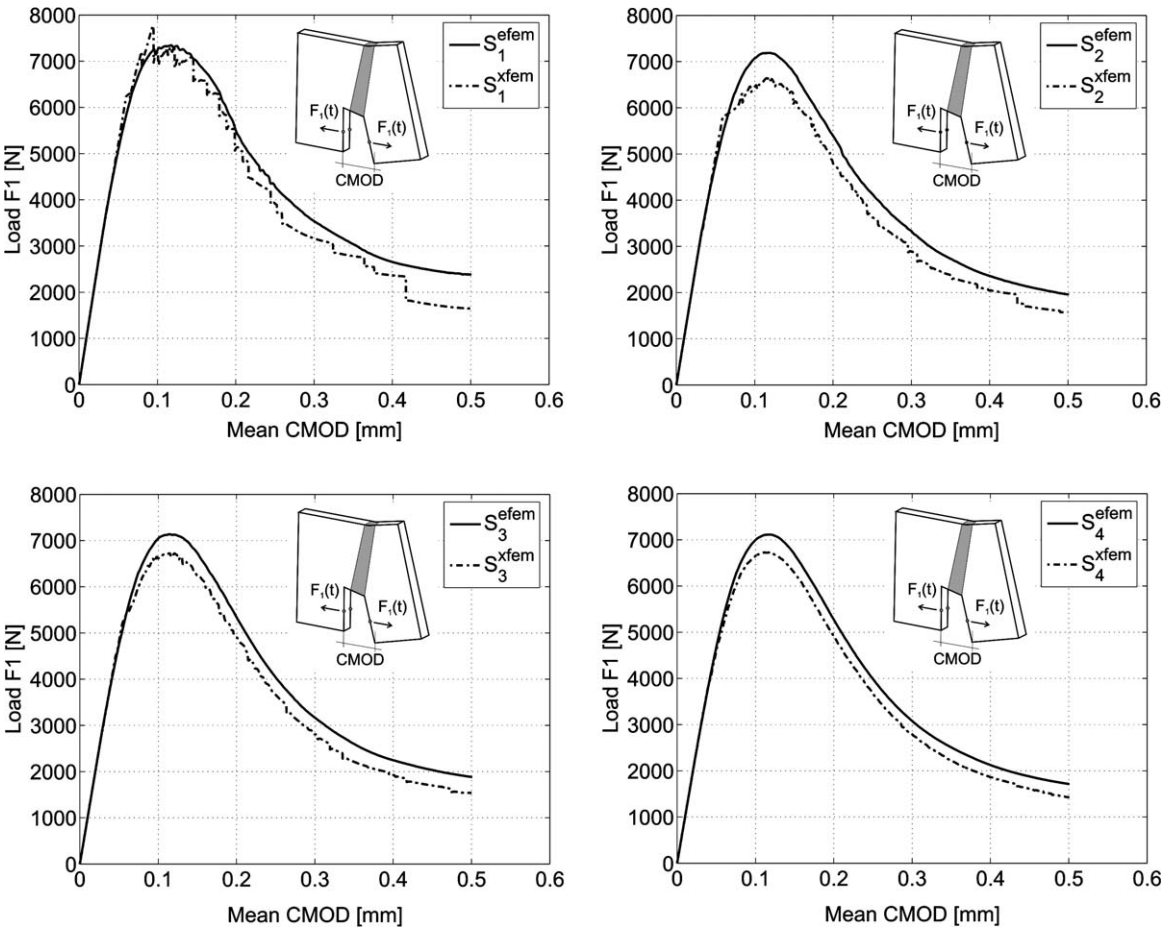

Fig. 12. 3D double-cantilever-beam (DCB) test with diagonal loads. Comparison of E-FEM and X-FEM solutions for every mesh of the sequence.

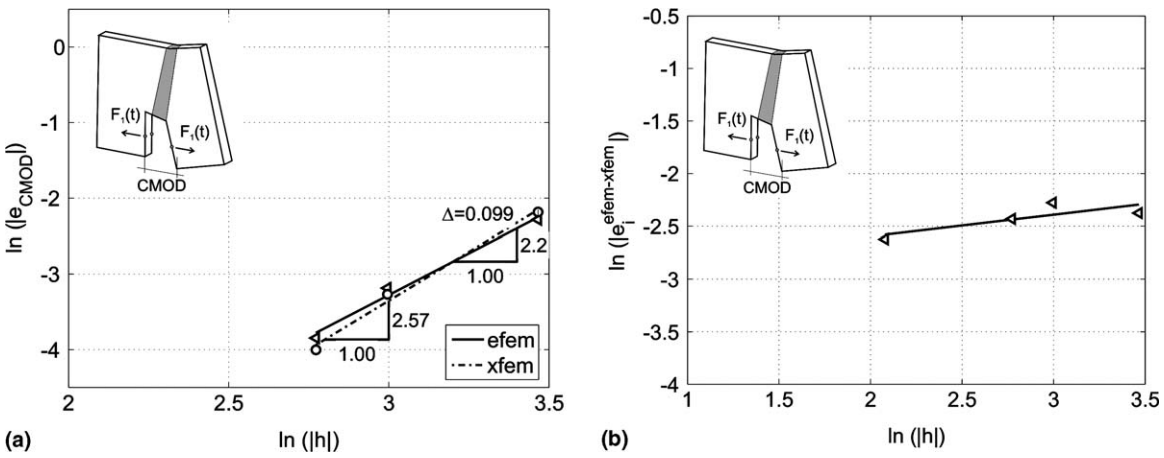

Fig. 13. 3D double-cantilever-beam (DCB) test with diagonal loads: (a) relative errors vs. element size and (b) E-FEM – X-FEM differences vs. element size h.

Fig. 11 displays the numerical solution of the structural response (F_1 loads vs. CMOD curves) for both, E-FEM and X-FEM procedures, using the four meshes. Fig. 12 shows one-to-one comparison of the solution obtained with both methods for every mesh.

Fig. 13 is devoted to evaluation of error and error convergence in L_2-*norm* in terms of the formulas in Eqs. (16) and (17). Again, they display the trend towards a unique solution also in this 3D case.

Finally, Table 2 compares both formulations in terms of the computational costs. It is remarkable that, for this 3D cases the relative computational cost, X-FEM/E-FEM, in the last column of the table, increases considerably with respect to 2D case.

4.2. Four points bending test

In order to extend the comparison to the case of modelling curved cracks, the classical problem of a single-edged notched beam supported in four points, shown in Fig. 14, is considered.

Table 2
3D double-cantilever-beam (DCB) test with diagonal loads

Finite element mesh (1)	*Nstep* (2)	Method (3)	Ne_i (4)	Ne_f (5)	*RNe* (6) = (5)/(4)	bw_i (7)	bw_f (8)	*Rbw* (9) = (8)/(7)	*Ta* [s] (10)	RCC (11)
Mesh 1 (763 elem.)	1200	E-FEM	797	797	1	62	62	1	136	2.55
		X-FEM	797	977	1.23	62	78	1.26	347	
Mesh 2 (2200 elem.)	1200	E-FEM	1760	1760	1	114	114	1	450	2.43
		X-FEM	1760	2165	1.23	114	146	1.28	1094	
Mesh 3 (3820 elem.)	1200	E-FEM	2787	2787	1	149	149	1	867	2.17
		X-FEM	2787	3357	1.20	149	184	1.23	1882	
Mesh 4 (25,137 elem.)	1200	E-FEM	14,958	14,958	1	448	448	1	16,628	1.50
		X-FEM	14,958	17,266	1.15	448	511	1.14	25,055	

Computational data and relative computational cost X-EFEM/E-FEM (RCC).

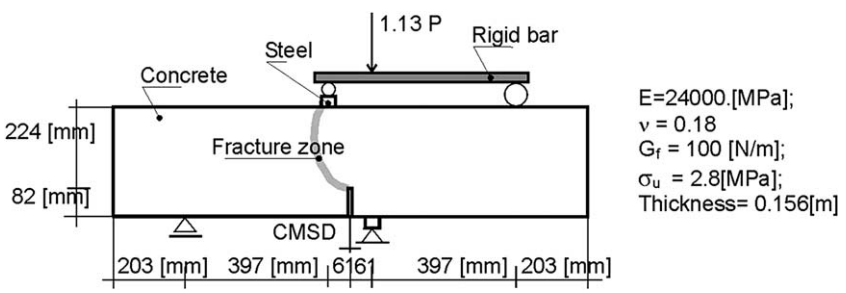

Fig. 14. Single-notched beam under four points bending test.

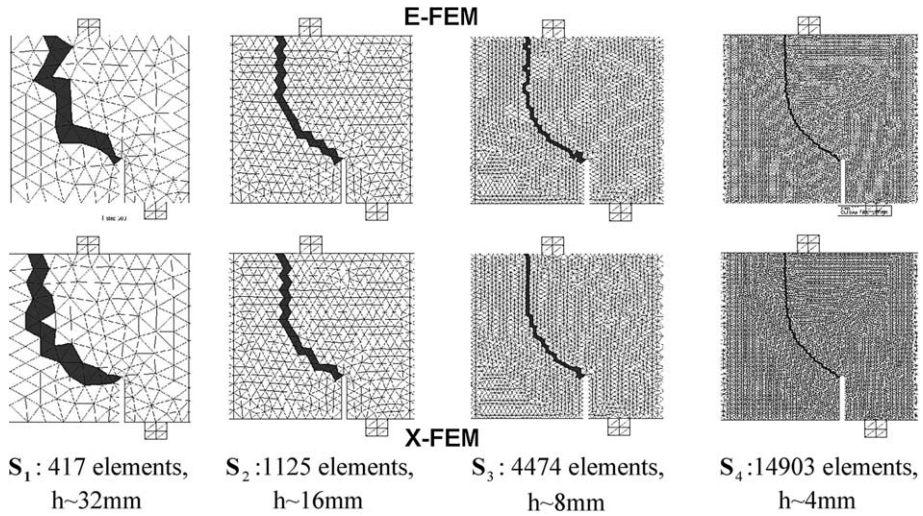

Fig. 15. 2D four points bending test. Finite element meshes in the cracked zone and captured discontinuity paths with E-FEM and X-FEM enrichments.

The numerical simulations, for both two- and three-dimensional cases, have been done without imposing, beforehand, the discontinuity path, which is obtained using the methodology presented in Section 3.3.

4.2.1. 2D modelling

The four meshes, displayed in Fig. 15, are considered for the analyzes defining the sequences $(\mathbf{S}_1,\mathbf{S}_2,\mathbf{S}_3,\mathbf{S}_4)$. Their average element sizes in the fracture zone are, respectively, $h = 32$, 16, 8 and 4 mm. The same figure shows the obtained discontinuity paths for both E-FEM and X-FEM enrichments (the elements crossed by the discontinuity path are shown in dark). It can be checked as the captured discontinuity path tends to be the same as the mesh is refined. The solution sequences $S^{\text{efem}} = \{S_1^{\text{efem}}, S_2^{\text{efem}}, S_3^{\text{efem}}, S_4^{\text{efem}}\}$, $S^{\text{xfem}} = \{S_1^{\text{xfem}}, S_2^{\text{xfem}}, S_3^{\text{xfem}}, S_4^{\text{xfem}}\}$ for the structural responses, (load P vs. CMSD) are plotted in Fig. 16 (for every enrichment in the complete mesh sequence) and in Fig. 17 (for both enrichments in the same mesh of the sequence). Fig. 18 refers to the relative errors provided by E-FEM and X-FEM and the relative L_2-*norm* of the differences of solutions.

Table 3 shows the comparative computational cost required for solving the different cases.

4.2.2. 3D modelling

The same problem is now solved using a 3D model and the four unstructured meshes of Fig. 19.

In Fig. 20, 3D four points bending test details about the obtained three-dimensional curved crack surface are presented.

Fig. 21 displays the sequences of solutions, with progressively refined meshes, supplied by the E-FEM and X-FEM procedures. The abscissa (CSMD) has been computed as the average value of CSMD along the specimen thickness.

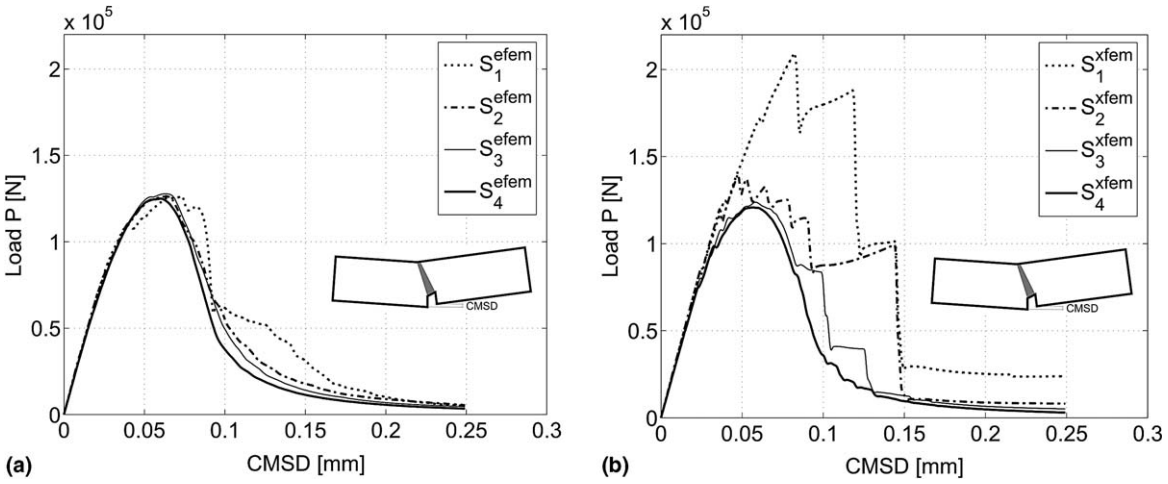

Fig. 16. 2D four points bending test. Load P vs. CMSD curves: (a) E-FEM and (b) X-FEM solutions.

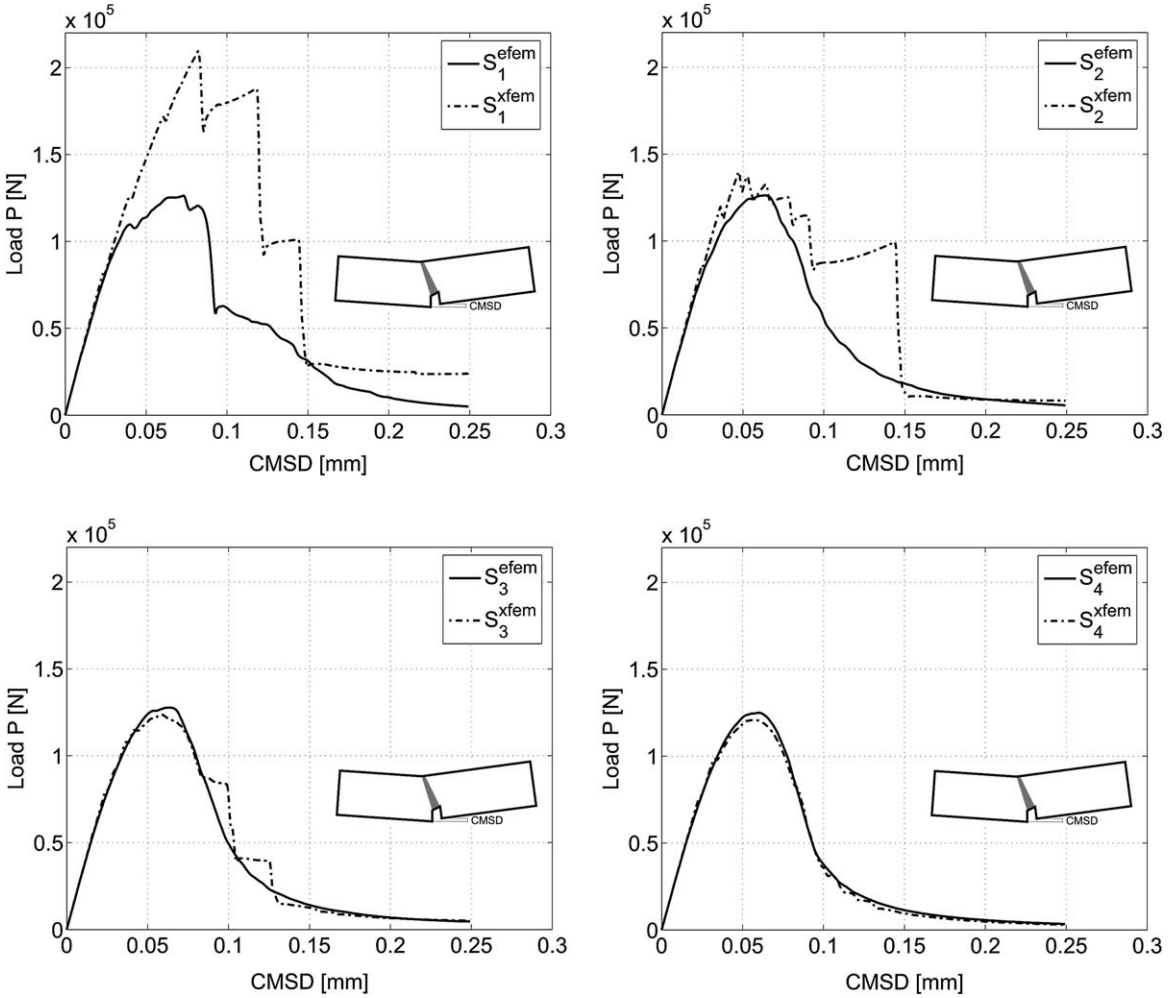

Fig. 17. 2D four points bending test. Load P vs. CMSD: comparison of E-FEM and X-FEM solutions for every mesh of the sequence.

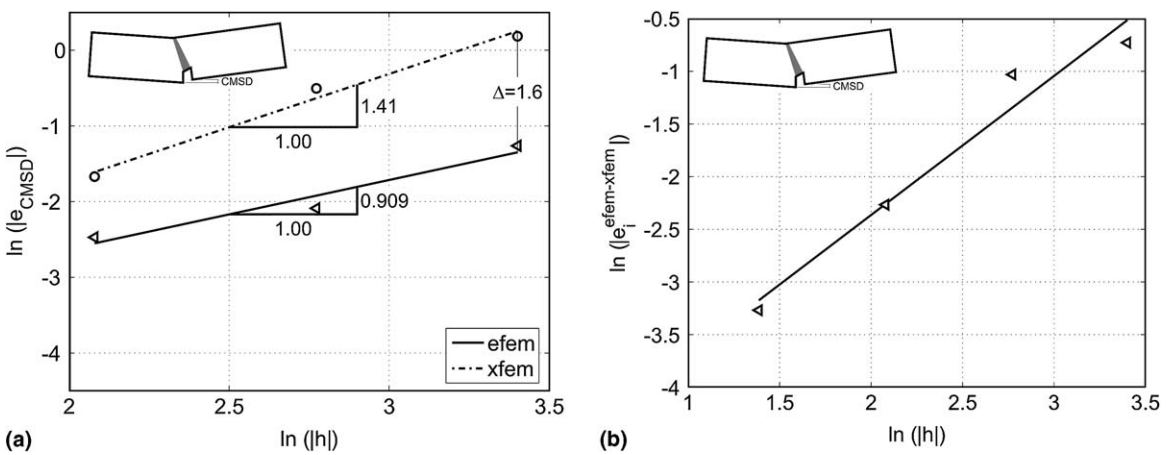

Fig. 18. 2D four points bending test: (a) relative errors vs. element size h and (b) E-FEM − X-FEM differences vs. element size h.

Fig. 22 compares the E-FEM vs. X-FEM solutions for the four different meshes and Fig. 23 displays the corresponding error and covergence curves with mesh refinement. Finally, Table 4 presents the comparative computational cost. Again it can be noticed a substantial increase of the computational cost ratios X-FEM/E-FEM in comparison with the 2D case in Table 3 (last columns).

Table 3
2D four points bending test

Finite element mesh (1)	*Nstep* (2)	Method (3)	Ne_i (4)	Ne_f (5)	*RNe* (6) = (5)/(4)	bw_i (7)	bw_f (8)	*Rbw* (9) = (8)/(7)	*Ta* [s] (10)	RCC (11)
Mesh 1 (417 elem.)	500	E-FEM	509	509	1	23	23	1	13.1	1.21
		X-FEM	509	559	1.10	23	26	1.13	15.9	
Mesh 2 (1125 elem.)	500	E-FEM	1235	1235	1	39	39	1	37.0	1.15
		X-FEM	1235	1311	1.06	39	42	1.08	42.7	
Mesh 3 (3922 elem.)	500	E-FEM	4683	4683	1	74	74	1	190	1.12
		X-FEM	4683	4841	1.03	74	78	1.05	212	
Mesh 4 (14,900 elem.)	500	E-FEM	15,161	15,161	1	138	138	1	1021	1.11
		X-FEM	15,161	15,507	1.02	138	143	1.04	1135	

Computational data and relative computational cost X-EFEM/E-FEM (RCC).

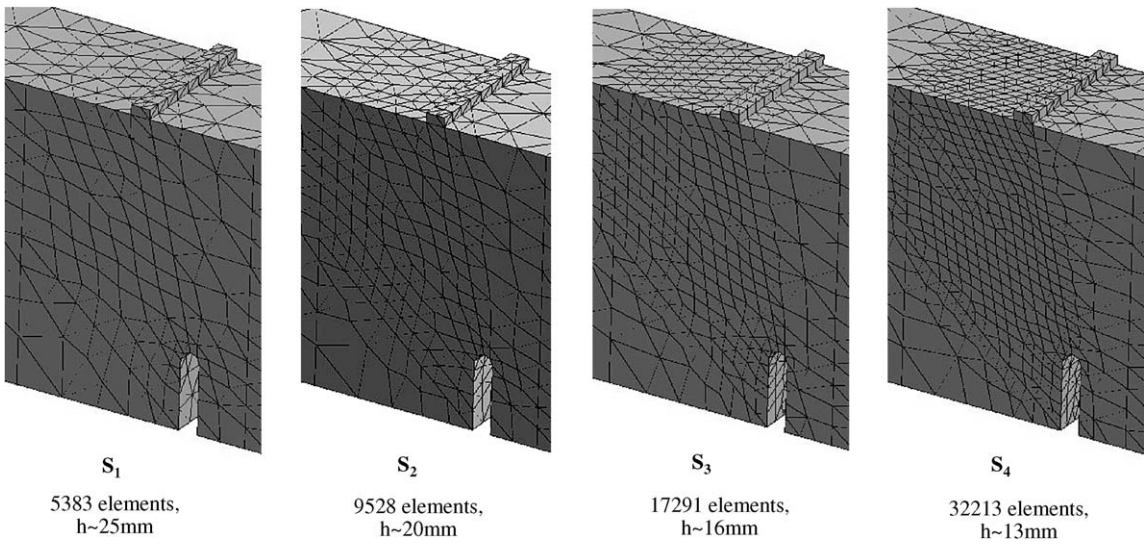

Fig. 19. 3D four points bending test. Mesh sequence ($\mathbf{S}_1$,$\mathbf{S}_2$,$\mathbf{S}_3$,$\mathbf{S}_4$).

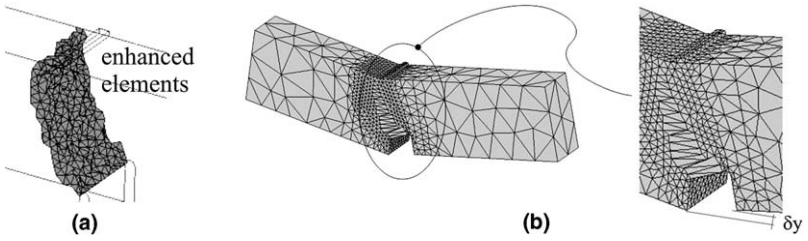

Fig. 20. 3D four points bending test: (a) elements intersected by the crack surface and (b) failure deformation mode.

4.3. Multifracture modeling. Composite material

The single fracture case considered so far is a very specific case, in material failure modeling, restricted to homogeneous materials in quasi-static problems. When the material is non-homogenous, as it happens in many cases of interest like in composite materials, multiple cracks can remain simultaneously active during long parts of the analysis. The purpose of this test is to check the relative performance of E-FEM and X-FEM for this case. Since the degree of accuracy and convergence does not substantially change from what has been shown in previous examples, the comparison is only presented in terms of the computational cost.

For this purpose the test displayed in Fig. 24 is used. It consists of a specimen of composite material made of a concrete matrix reinforced by steel bars distributed across the height as elastic steel layers. The specimen is increasingly pulled horizontally from the right end, and a number of vertical cracks appear. Their separation and, therefore, the number of cracks, depends on the amount of reinforcement with respect to concrete and their relative bonding [3,14]. For the simulation, and

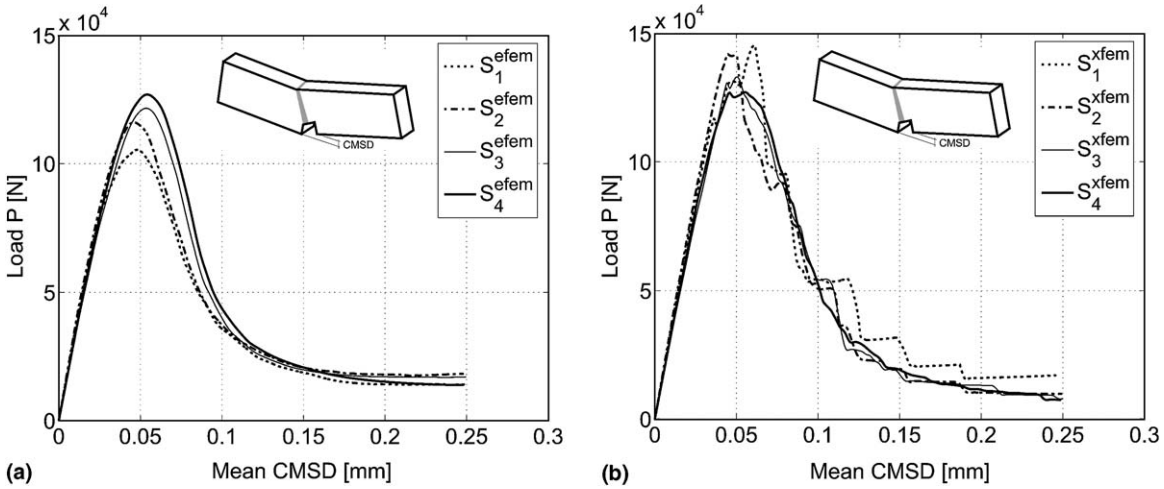

Fig. 21. 3D four points bending test. Load P vs. CMSD curves: (a) E-FEM and (b) X-FEM solutions.

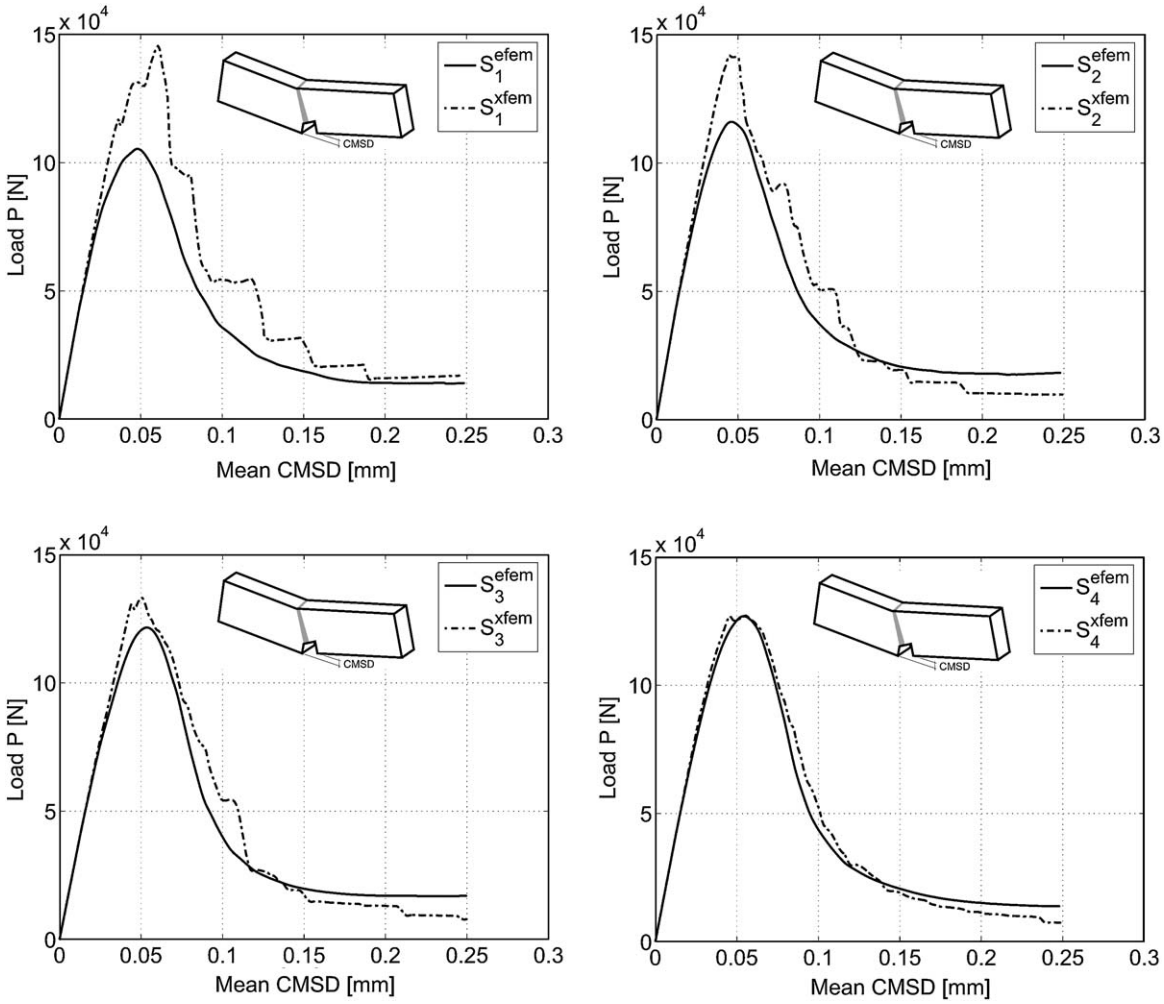

Fig. 22. 3D four points bending test. Load P vs. CMSD: comparison of E-FEM and X-FEM solutions for every mesh of the sequence.

since perfect concrete/steel bonding has been considered, that number of cracks has been artificially imposed by perturbing the concrete peak stress in the appropriate number of vertical layers of elements. The mechanical properties of concrete are: $E = 27{,}350$ MPa (Young's modulus), $\nu = 0$ (Poisson's ratio), $G_f = 100$ N/m (fracture energy), $\sigma_u = 3.19$ MPa (ultimate

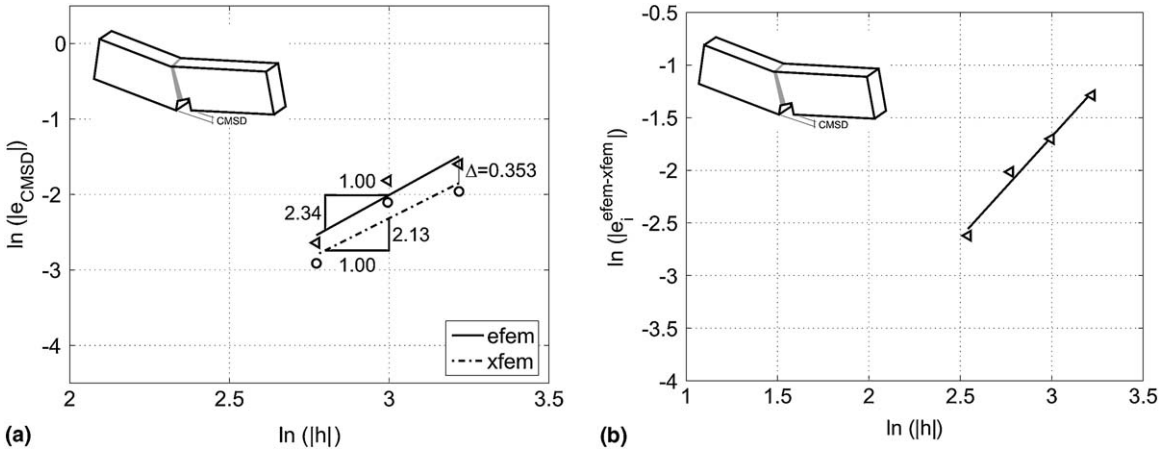

Fig. 23. 3D four points bending test: (a) relative errors vs. element size h and (b) E-FEM − X-FEM differences vs. element size h.

Table 4
3D four points bending test

Finite element mesh (1)	*Nstep* (2)	Method (3)	Ne_i (4)	Ne_f (5)	*RNe* (6) = (5)/(4)	bw_i (7)	bw_f (8)	*Rbw* (9) = (8)/(7)	*Ta* [s] (10)	RCC (11)
Mesh 1 (5383 elem.)	400	E-FEM	3768	3768	1	237	237	1	635	2.00
		X-FEM	3768	4389	1.16	237	290	1.22	1271	
Mesh 2 (9528 elem.)	400	E-FEM	6096	6096	1	431	431	1	2431	1.96
		X-FEM	6096	7089	1.16	431	566	1.31	4757	
Mesh 3 (17,291 elem.)	400	E-FEM	10,401	10,401	1	524	524	1	5400	1.56
		X-FEM	10,401	11,967	1.15	524	628	1.20	8398	
Mesh 4 (32,213 elem.)	178	E-FEM	18,479	18,479	1	833	833	1	8818	1.38
		X-FEM	18,479	20,903	1.13	833	963	1.16	12,135	

Computational data and relative computational cost X-EFEM/E-FEM (RCC).

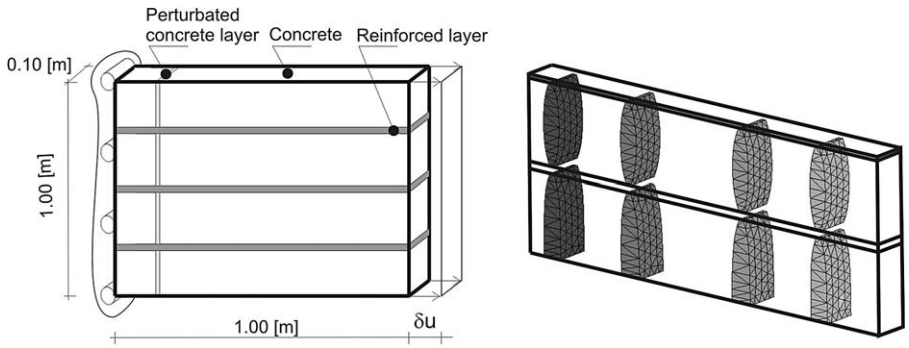

Fig. 24. Reinforced concrete specimen. Geometry and deformed sets of elements capturing the vertical cracks. Number of elements 23,245, $h \sim 26$ mm.

tensile strength). The reinforcing steel properties are $E = 210{,}000$ MPa and $v = 0$. Due to symmetry only the lower half of the specimen has been modeled.

Four different cases, corresponding to 2, 4, 6 and 8 developed cracks, have been analyzed using the E-FEM and X-FEM procedures. The corresponding computational costs, broken down into the main parts of the code (residual forces, stiffness matrix, solver and total computational costs) have been tracked and plotted, in Fig. 25, for an increasing number of cracks. There, it can be noticed that

- The E-FEM computational costs keep almost constant with the number of cracks. This could have been expected, since the additional degrees of freedom associated to the elemental displacement jumps are condensed out, and they do not substantially contribute to the computational costs, irrespective of their number.

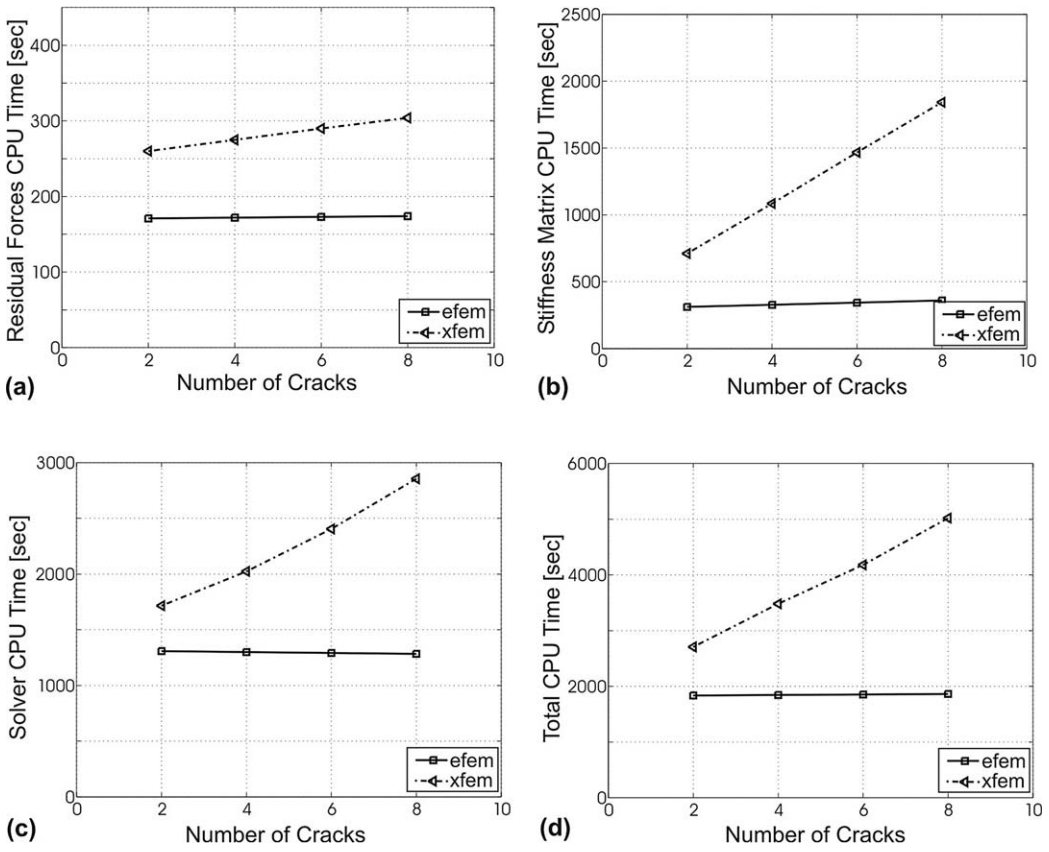

Fig. 25. Reinforced concrete plate. Computational CPU time as a function of the crack number for different parts of the simulation procedure: (a) residual evaluation and assembly; (b) stiffness matrix evaluation and assembly; (c) solving the linearized system of equations and (d) total computational cost.

- The X-FEM computational cost is always larger than the corresponding in E-FEM and grows linearly with the number of modeled cracks. The most affected operations are the stiffness matrix construction and the solver (in turn the most time consuming operations). This should also be expected since the additional nodal degrees of freedom are not condensed in this case.
- As a result, the relative computational cost X-FEM/E-FEM grows linearly with the number of modeled cracks.

5. Conclusions

Along this work a comparison of nodal (X-FEM) and elemental (E-FEM) enrichments in finite elements for capturing strong discontinuities has been done. Both enrichments have been implemented in the same finite element code, on the basis of optimized algorithms and coding, and tested on a set of 2D and 3D examples under exactly the same conditions. The obtained results can be summarized as follows:

- When implemented on the basis of the same element (linear triangles and linear tetrahedra in this study), *both formulations converge to the same results*, either the qualitative (captured discontinuity paths) or the quantitative ones.
- The *rate of convergence of both enrichments is similar*. Substantial differences in terms of convergence rates, in L_2-norms, have not been found (for both cases the convergence rates are fairly superior to linear).
- Therefore, unlike what some times has been asserted, *the different kind of interpolation of the displacement jump* provided by both types of enrichments (linear for X-FEM, element wise constant for E-FEM) *does not affect neither the accuracy of the representation of the discontinuity nor the convergence rate. Neither the fact that X-FEM, unlike E-FEM, allows discontinuous elemental regular strains across the discontinuity interface seems to affect the accuracy and convergence rates.* They rather seem to be dependent on the degree of interpolation for the standard displacement modes of the chosen basic element (linear in this study).
- It has been observed that, for rather coarse meshes, both the accuracy and the smoothness of the response are generally higher with the E-FEM formulation. More specifically: the response curves corresponding to X-FEM exhibit, as compared with those with E-FEM, a more abrupt shape and jumps *that can be associated to the relative delay of the former in*

the activation of the degrees of freedom of the enriching modes as a new element is crossed by the crack path. This effect, that can be also observed to a lesser extent in the E-FEM results, diminishes with the mesh refinement and also appears in the results provided by other authors using X-FEM [9,35]. It has been reported the addition of new enriching modes at the crack tip [37] that might, at least partially, correct this response, but this type of techniques, that belong to a higher level of sophistication and that are still under development [12], has not been applied here in none of the E-FEM and X-FEM formulations.

- *Computational costs are, in all cases, favourable to the E-FEM enrichment*. For single crack modelling X-FEM is 1.1–1.2 times (in 2D cases) and 1.3–2.5 times (in 3D cases) more expensive than E-FEM. These ratios decrease with increasing levels of discretizations. The reasons for the higher cost for X-FEM seem to be the additional, not condensable at elemental level, degrees of freedom and the higher order integration necessary in X-FEM. Certainly, those figures should be taken as a trend, since they could be modified in any sense by alternative implementations. They correspond to the best implementation knowledge of the authors, after a substantial coding effort in a reasonably well-checked finite element code.
- As for multiple cracking modelling, the *computational costs associated to the E-FEM enrichment remain almost constant for increasing number of cracks*. On the contrary, for *the X-FEM enrichment, the computational cost increases linearly with the number of involved cracks*. For the considered 3D case this increase is up to around 20% of the total cost per every additional crack.
- *In the context of the implicit/explicit integration of the constitutive model both formulations are very robust*. All simulations have been conducted beyond the critical loads and up to almost complete exhaustion of the loading capacity.

In summary, *from the specific comparison setting devised for this study, based on standard formulations of both methods and their optimized implementations and coding*, the main differences are: (a) the higher relative computational cost of X-FEM with respect to E-FEM, associated to the possibility of condensation at elemental level in E-FEM and the higher integration order in X-FEM, and (b) the higher accuracy in E-FEM, mainly for coarse meshes. Anyhow, both methods are amenable to be reformulated and improved, which could define different scenarios for which the corresponding comparison studies should be done.

Acknowledgements

Financial support from the Spanish Ministry of Science and Technology, through Grant BIA 2004-02080, and from the Catalan Government Research Department, through the CIRIT Grant 2001-SGR 00262, is gratefully acknowledged.

The third author was supported by the Programme Alban, the European Union Programme of High Level Scholarships for Latin American, scholarship, Ref. No. E04D035536AR.

References

[1] J. Alfaiate, New developments in the study of strong embedded discontinuities infinite elements, Adv. Fract. Damage Mech. 251–252 (2003) 109–114.
[2] F. Armero, K. Garikipati, An analysis of strong discontinuities in multiplicative finite strain plasticity and their relation with the numerical simulation of strain localization in solids, Int. J. Solids Struct. 33 (1996) 2863–2885.
[3] Z. Bazant, L. Cedolin, Fracture mechanics of reinforced concrete, J. Eng. Mech. Div. ASCE (1980) 1287–1305.
[4] T. Belytschko, H. Chen, J.X. Xu, G. Zi, Dynamic crack propagation based on loss of hyperbolicity and a new discontinuous enrichment, Int. J. Numer. Methods Engrg. 58 (2003) 1873–1905.
[5] T. Belytschko, N. Moes, S. Usui, C. Parimi, Arbitrary discontinuities in finite elements, Int. J. Numer. Methods Engrg. 50 (2001) 993–1013.
[6] C. Feist, G. Hofstetter, Computational aspects of concrete fracture simulations in the framework of the SDA. Presented at Fracture Mechanics of Concrete Structures FRAMCOS 2004, Vale, Co, USA, 2004.
[7] K. Garikipati, T.J.R. Hughes, A study of strain-localization in a multiple scale framework. The one dimensional problem, Comput. Methods Appl. Mech. Engrg. 159 (1998) 193–222.
[8] T.C. Gasser, G.A. Holzapfel, Geometrically non-linear and consistently linearized embedded strong discontinuity models for 3D problems with an application to the dissection analysis of soft biological tissues, Comput. Methods Appl. Mech. Engrg. 192 (2003) 5059–5098.
[9] T.C. Gasser, G.A. Holzapfel, Modeling 3D crack propagation in unreinforced concrete using PUFEM, Comput. Methods Appl. Mech. Engrg. 194 (2005) 2859–2896.
[10] M. Jirasek, Comparative study on finite elements with embedded discontinuities, Comput. Methods Appl. Mech. Engrg. 188 (2000) 307–330.
[11] A.S. Kobayashi, M.N. Hawkins, D.B. Barker, B.M. Liaw, Fracture process zone of concrete, in: S.S.P. (Ed.), Application of Fracture Mechanics to Cementitious Composites, Marinus Nujhoff Publ., Dordrecht, 1985, pp. 25–50.
[12] P. Laborde, J. Pommier, Y. Renard, M. Salaün, High order extended finite element method for cracked domains. Presented at Computational Plasticity VIII: Fundamentals and Applications, Barcelona, Spain, 2005.
[13] R. Larsson, K. Runesson, N.S. Ottosen, Discontinuous displacement approximation for capturing plastic localization, Int. J. Numer. Methods Engrg. 36 (1993) 2087–2105.
[14] K. Liao, K.L. Reifsnider, A tensile strength model for unidirectional fiber-reinforced brittle matrix composite, Int. J. Fract. 106 (2000) 95–115.
[15] M. Cervera, C. Agelet, M. Chiumenti, COMET: A Multipurpose Finite Element Code for Numerical Analysis in Solid Mechanics, Technical University of Catalonia (UPC), 2001.

[16] S. Mariani, U. Perego, Extended finite element method for quasi-brittle fracture, Int. J. Numer. Methods Engrg. 58 (2003) 103–126.
[17] N. Moës, N. Sukumar, B. Moran, T. Belytschko, An extended finite element method (X-FEM) for two and three-dimensional crack modelling. Presented at ECCOMAS 2000, Barcelona, Spain, 2000.
[18] J. Mosler, G. Meschke, 3D modelling of strong discontinuities in elastoplastic solids: fixed and rotating localization formulations, Int. J. Numer. Methods Engrg. 57 (2003) 1553–1576.
[19] J. Mosler, G. Meschke, Embedded crack vs. smeared crack models: a comparison of elementwise discontinuous crack path approaches with emphasis on mesh bias, Comput. Methods Appl. Mech. Engrg. 193 (2004) 3351–3375.
[20] J. Oliver, Modelling strong discontinuities in solid mechanics via strain softening constitutive equations. 2. Numerical simulation, Int. J. Numer. Methods Engrg. 39 (1996) 3601–3623.
[21] J. Oliver, On the discrete constitutive models induced by strong discontinuity kinematics and continuum constitutive equations, Int. J. Solids Struct. 37 (2000) 7207–7229.
[22] J. Oliver, A.E. Huespe, Continuum approach to material failure in strong discontinuity settings, Comput. Methods Appl. Mech. Engrg. 193 (2004) 3195–3220.
[23] J. Oliver, A.E. Huespe, Theoretical and computational issues in modelling material failure in strong discontinuity scenarios, Comput. Methods Appl. Mech. Engrg. 193 (2004) 2987–3014.
[24] J. Oliver, A.E. Huespe, S. Blanco, D.L. Linero, Stability and robustness issues in numerical modeling of material failure in the strong discontinuity approach, Comput. Methods Appl. Mech. Engrg. accepted for publication.
[25] J. Oliver, A.E. Huespe, M.D.G. Pulido, S. Blanco, Recent advances in computational modelling of material failure. Presented at 4th European Congress on Computational Methods in Applied Sciences and Engineering (ECCOMAS 2004), University of Jyväskylä, Jyväskylä, Finland, 2004.
[26] J. Oliver, A.E. Huespe, M.D.G. Pulido, S. Blanco, D. Linero, New developments in computational material failure mechanics. Presented at Sixth World Congress on Computational Mechanics (WCCM VI), Beijing, PR China, 2004.
[27] J. Oliver, A.E. Huespe, M.D.G. Pulido, E. Chaves, From continuum mechanics to fracture mechanics: the strong discontinuity approach, Engrg. Fract. Mech. 69 (2002) 113–136.
[28] J. Oliver, A.E. Huespe, E. Samaniego, A study on finite elements for capturing strong discontinuities, Int. J. Numer. Methods Engrg. 56 (2003) 2135–2161.
[29] R.L. Borja, R.A. Regueiro, A finite element model for strain localization analysis of strongly discontinuous fields based on standard Galerkin approximation, Comput. Methods Appl. Mech. Engrg. (2000) 1529–1549.
[30] J.G. Rots, Computational Modeling of Concrete Fractures, Delft University of Technology, 1988.
[31] K. Runesson, Z. Mroz, A note on nonassociated plastic flow rules, Int. J. Plast. 5 (1989) 639–658.
[32] J. Simo, J. Oliver, F. Armero, An analysis of strong discontinuities induced by strain-softening in rate-independent inelastic solids, Comput. Mech. 12 (1993) 277–296.
[33] A. Simone, Partition of unity-based discontinuous elements for interface phenomena: computational issues, Commun. Numer. Methods Engrg. 20 (2004) 465–478.
[34] B.W. Spencer, P.B. Shing, Rigid-plastic interface for an embedded crack, Int. J. Numer. Methods Engrg. 56 (2003) 2163–2182.
[35] G.N. Wells, L.J. Sluys, A new method for modelling cohesive cracks using finite elements, Int. J. Numer. Methods Engrg. 50 (2001) 2667–2682.
[36] K. Willam, N. Sobh, Bifurcation analysis of tangential material operators, in: G.N. Pande, J. Middleton (Eds.), Transient/Dynamic Analysis and Constitutive Laws for Engineering Materials, vol. 2, Martinus-Nijhoff Publishers, 1987, pp. C4/1–C4/13.
[37] G. Zi, T. Belytschko, New crack-tip elements for XFEM and applications to cohesive cracks, Int. J. Numer. Methods Engrg. 57 (2003) 2221–2240.